Fibrils Connect Microtubule Tips with Kinetochores: A Mechanism to Couple Tubulin Dynamics to Chromosome Motion

J. Richard McIntosh,[1,*] Ekaterina L. Grishchuk,[1,2] Mary K. Morphew,[1] Artem K. Efremov,[1,3] Kirill Zhudenkov,[3] Vladimir A. Volkov,[1,3] Iain M. Cheeseman,[4] Arshad Desai,[5] David N. Mastronarde,[1] and Fazly I. Ataullakhanov[3,6,7]

[1]Department of M.C.D. Biology, University of Colorado, Boulder, CO 80309-0347, USA
[2]Institute of General Pathology and Pathophysiology, 125315 Moscow, Russia
[3]National Research Center for Hematology, 117513 Moscow, Russia
[4]Whitehead Institute, Massachusetts Institute of Technology, Cambridge, MA 02139, USA
[5]Ludwig Institute for Cancer Research and Department of Cellular & Molecular Medicine, University of California,
San Diego, La Jolla, CA 92093, USA
[6]Physics Department, Moscow State University, 119899 Moscow, Russia
[7]Center for Theoretical Problems of Physicochemical Pharmacology, RAS, 119991 Moscow, Russia
*Correspondence: richard.mcintosh@colorado.edu
DOI 10.1016/j.cell.2008.08.038

SUMMARY

Kinetochores of mitotic chromosomes are coupled to spindle microtubules in ways that allow the energy from tubulin dynamics to drive chromosome motion. Most kinetochore-associated microtubule ends display curving "protofilaments," strands of tubulin dimers that bend away from the microtubule axis. Both a kinetochore "plate" and an encircling, ring-shaped protein complex have been proposed to link protofilament bending to poleward chromosome motion. Here we show by electron tomography that slender fibrils connect curved protofilaments directly to the inner kinetochore. Fibril-protofilament associations correlate with a local straightening of the flared protofilaments. Theoretical analysis reveals that protofilament-fibril connections would be efficient couplers for chromosome motion, and experimental work on two very different kinetochore components suggests that filamentous proteins can couple shortening microtubules to cargo movements. These analyses define a ring-independent mechanism for harnessing microtubule dynamics directly to chromosome movement.

INTRODUCTION

Mitotic spindle microtubules (MTs) and their associated proteins (MAPs) interact with kinetochores to ensure the accurate segregation of eukaryotic chromosomes. The interface between MTs and a kinetochore provides a firm attachment that can generate force for chromosome motion, either toward or away from the associated spindle pole. This interface is also a site where MTs can either add or lose tubulin subunits as chromosomes move, so it is significant for normal mitosis (Rieder and Salmon,

1998). Identification of the proteins that provide these functions is now well advanced in budding yeast (Westermann et al., 2007) and higher eukaryotes (Cheeseman and Desai, 2008; Liu et al., 2006). Several motor enzymes contribute to chromosome segregation, but MT depolymerization in vitro, even in the absence of soluble nucleotides, can mimic chromosome-to-pole motion in vivo (Coue et al., 1991; Koshland et al., 1988). Moreover, minus-end-directed motors are dispensable for poleward chromosome motion in yeasts (Grishchuk and McIntosh, 2006; Tanaka et al., 2007), suggesting that the root of chromosome movement lies in MT dynamics, not motor activity.

MT shortening can generate force because tubulin dynamics are associated with GTP hydrolysis. Tubulin-bound GTP is hydrolyzed shortly after polymerization, so most of the MT wall is GDP-tubulin. Surprisingly, GDP-tubulin will not polymerize, probably because its shape does not fit the MT lattice (Wang and Nogales, 2005). Assembled GDP-tubulin is therefore strained by interactions with its neighbors in the MT wall. This strain is relieved during depolymerization when strands of tubulin dimers, called protofilaments (PFs), become flared at the MT end (Mandelkow et al., 1991); presumably this PF shape reveals the minimum energy configuration of GDP tubulin, whereas GTP tubulin PFs are comparatively straight (Chretien et al., 1995; Muller-Reichert et al., 1998). Thus, the morphology of a MT end in vitro reflects its polymerization state.

PF bending during MT shortening has been proposed to do mechanical work (Koshland et al., 1988). Indeed, microbeads coupled to MTs by static links, e.g., a MAP or a biotin-streptavidin bond, experience a brief tug during PF bending (Grishchuk et al., 2005). Cargo that is bound to MTs by either motor enzymes (Lombillo et al., 1995b) or an encircling protein complex (Westermann et al., 2006) will move processively during MT shortening in vitro, even without ATP. Thus, if kinetochores were harnessed to MTs with the right "couplers," the energy liberated by tubulin depolymerization could drive chromosome-to-pole motion (Efremov et al., 2007; Hill, 1985; Molodtsov et al., 2005). This raises the question of how kinetochores take advantage of
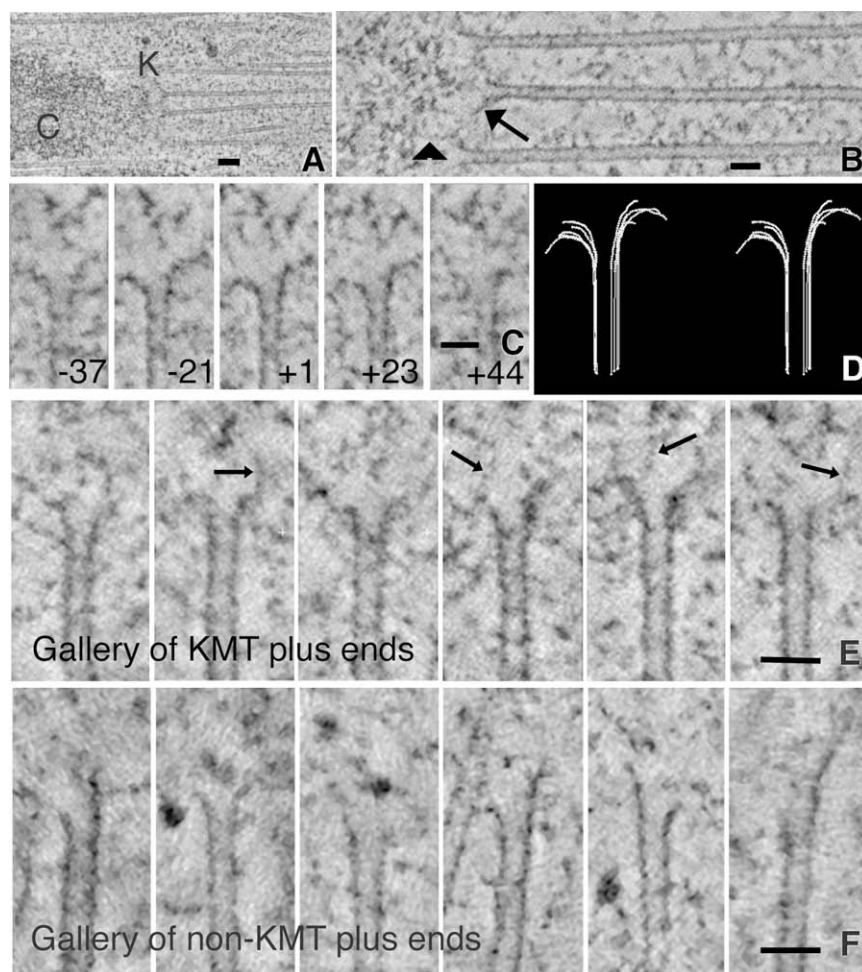
Figure 1. Microtubules from Mitotic PtK₁ Cells

(A) Average of 15 consecutive tomographic slices, total thickness ~30 nm, analogous to a conventional thin section. Chromosome (C) and kinetochore (K) show characteristic staining. MTs were identified as KMTs when they ended in a cluster near a chromosome. Bar = 0.1 μm.

(B) KMTs from the same cell but seen in a ~2 nm slice cut parallel to their axes with the "Slicer" feature of IMOD. Arrow identifies a bending PF; arrowhead indicates a fibril that runs from a PF to the chromatin. Bar = 0.05 μm.

(C) Multiple image planes that contain the MT axis but are oriented at the angles stated relative to the plane of section; PFs in each view differ in length and extent of flare. Bar = 0.05 μm.

(D) Stereo pair of a 3D model of all the PFs traced on the MT shown in Figure 1C. Use wall-eyed viewing.

(E) Gallery of different KMT ends from the same cell. PF flare is variable; fibrillar material is associated with some PFs (arrows). Bar = 0.05 μm.

(F) Gallery of non-KMT ends from the polar region of a metaphase spindle; no chromosomes are near. Some MT ends are flared, others not; fibrils are not seen. Bar = 0.05 μm.

the depolymerization machinery to facilitate chromosome segregation.

Kinetochore structure has been studied for years, but most kinetochores are so small that informative early work has been done either by immuno light microscopy or electron microscopy. Recent light microscopy has localized tagged kinetochore components along the spindle axis with almost nanometer precision (Joglekar et al., 2008; Schittenhelm et al., 2007), but electron microscopy has defined the image of kinetochores that most scientists consider. With this method, vertebrate chromosomes show kinetochore-associated MTs (KMTs) penetrating a darkly staining "outer plate" (Rieder and Salmon, 1998), which has commonly been interpreted as the principal MT-chromosome connection. Electron tomography of well-preserved kinetochores in PtK₁ cells has refined this description as a meshwork of fibers that connect adjacent KMTs to one another and to nearby chromatin (Dong et al., 2007). PFs at the ends of many KMTs flare as they penetrate this plate and approach the chromatin (VandenBeldt et al., 2006). The fraction of KMTs with flared ends appears greater during anaphase than metaphase, perhaps a reflection of increased MT depolymerization in anaphase. However, ~70% of metaphase KMTs have flared ends, which poses an enigma: why do so many KMTs appear to be

depolymerizing when their lengths are, on average, constant? Is KMT PF flare a simple reflection of dynamic state, as in vitro, or do other factors affect PF curvature in vivo?

To address these questions and to develop a more complete picture of the kinetochore-MT interface, we have used electron tomography to study the three-dimensional (3D) structure of individual PFs at the plus ends of MTs from mitotic PtK₁ cells, obtaining quantitative information about the curvature of PFs from several kinds of MTs. Approximately half of the PFs at KMT plus ends curve differently from those on either polymerizing or depolymerizing MTs in vitro. Our data suggest that these shapes do not result simply from MT dynamics but from associations between PFs and kinetochore-associated fibrils. These fibrils appear to impede PF bending, suggesting a mechanism for converting the energy of MT depolymerization into chromosome movement. This hypothesis is supported by a theoretical analysis of the effects of force on PF curvature and by observations that implicate two fibrillar, kinetochore-associated proteins as couplers between cargo and MT depolymerization in vitro.

RESULTS

Electron Tomography Provides Sufficient Resolution to Characterize PF Shape at MT Ends

The structure of a kinetochore and its relationship to spindle MTs can be visualized in electron tomograms (Figure 1A), which permit clear distinctions between KMTs and other MTs that do not associate with kinetochores (non-KMTs). Most PFs at the
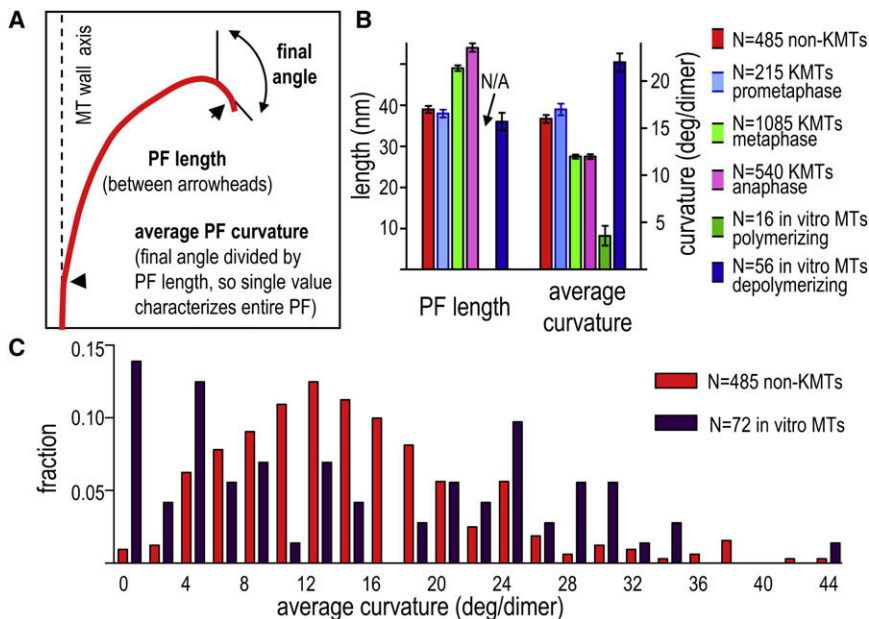
Figure 2. Quantitative Analysis of Average PF Shape

(A) Diagram of a traced PF and the ways the *how-flared* program identified its length, final angle, and average curvature.

(B) Average properties of PFs from non-KMTs, KMTs at several mitotic stages, and MTs in vitro. N = number of PFs for each MT class. N/A = not applicable. Error bars here and on all graphs are standard errors of the means (SEMs).

(C) Histogram of average PF curvature for non-KMTs (red) and pooled samples of P- and D-MTs in vitro (dark red). N = number of PFs in each class.

plus ends of KMTs show "flare," i.e., they bend away from the MT axis (O'Toole et al., 1999, 2003; VandenBeldt et al., 2006; Figure 1B and Movie S1 available online). We have examined 4–8 PFs at the end of each MT within the ~1 μm³ of cellular volume reconstructed in each of 23 tomograms (2325 spindle PFs in total). Figures 1C and 1D portray a single prometaphase KMT plus end in tomographic slices cut at different orientations through its axis; the flares of its PFs are evident. Additional examples of KMTs from cells in prometaphase (Figure 1E and Movie S2), metaphase, and anaphase (Figure S1 and Movies S3 and S4) demonstrate that PF flare is extensive throughout mitosis.

The Plus Ends of KMTs Are Initially Like Those of Non-KMTs, but during Mitosis Their PFs Become Longer and Less Curved

To ask whether MT ends showed systematic variations in shape we have compared tomograms of different places in spindles and times in mitosis. The plus ends of non-KMTs displayed a mixture of flared and straight PFs (Figure 1F). To compare these MTs with KMTs, we determined the length of the flare on each PF, the orientation of its final segment, and its average curvature (Figure 2A). With any of these measures, PF flare on a single MT was variegated (Table 1): all KMTs contained some PFs that were widely flared, and most included others that were rather straight. The variability among the PFs from all the MTs of a single kinetochore was similar to that of PFs from a single MT (Table 1). Variation in PF flare is not likely to be an artifact of our sample preparation techniques (Supplemental Text), but it was sufficiently great that large numbers of PFs were required to identify statistically significant differences between MTs from different biological contexts (Supplemental Text and Tables S1–S3 and S7). Thus, we have compared PFs by using the mean values for all the PFs in one category. With this approach, mean PF structure from KMT plus ends in early mitosis was similar to that of non-KMTs, but as mitosis proceeded, KMT PFs became longer, and their average curvatures decreased (Figure 2B).

Many PFs on Spindle MTs Are Different from Those on MTs Formed In Vitro

Changes in mean flare during mitotic progression suggested that PFs might play a direct role in chromosome segregation, so we compared PF flares in vivo with those of MTs with known dynamic state, using images of MTs that had been grown from pure tubulin in vitro and described in the literature. Most PFs on polymerizing MTs (P-MTs) do not project beyond their neighbors and do not flare, so these MT ends are commonly blunt (Mandelkow et al., 1991). A few growing PFs are longer than their neighbors, extending by highly variable amounts that depend on conditions (Chretien et al., 1995; Muller-Reichert et al., 1998). The mean (± standard deviation [SD]) of their average curvatures was, however, reasonably consistent: 3.6 ± 4.2°/dimer. PFs on "D-MTs," i.e., those depolymerized by either subunit dilution or a drop in temperature (Chretien et al., 1995; Mandelkow et al., 1991), showed a mean curvature of 22 ± 7°/dimer and a mean length of 36 ± 16 nm (Figure 2B).

Previous studies of KMT ends in vivo have described PFs as similar to those in vitro (VandenBeldt et al., 2006), but our quantitative methods have found differences. Whereas PF lengths in prometaphase and metaphase were similar to those of D-MTs, their mean average curvatures fell between those of P- and D-MTs in vitro (Figure 2B). This might, of course, be because in vivo populations are mixtures of growing and shrinking MTs. However, a histogram of average PF curvatures for pooled P- and D-MTs in vitro showed two peaks, while comparable data from non-KMTs in vivo showed only one broad distribution (Figure 2C). Thus, the structure of MT ends in mitotic cells differs from that seen in vitro.

PF Fine Structure as an Indicator of MT Dynamics

Since the unique features of mitotic MT end structure might reflect function in chromosome segregation, we worked to understand the details of PF flare, not just its average

Table 1. Typical Average PF Structures

MT#	PF#	Length (nm)	Final Ang (deg)	Avg. Curv. (deg/dimer)
Eight PFs from One Prometaphase KMT Numbers Are Parameters for Each PF				
1	1	48	114	20
	2	34	125	29
	3	35	64	15
	4	61	159	21
	5	13	35	21
	6	21	38	14
	7	97	178	15
	8	23	76	26
Mean		41	98	20
SD		27	53	5.5
63 PFs from 9 prometaphase KMTs. Numbers are means for all PFs from each MT.				
1	1–8	41	98	20
2	1–6	36	77	35
3	1–8	35	83	21
4	1–8	35	82	19
5	1–6	44	104	19
6	1–7	36	100	22
7	1–8	33	84	21
8	1–6	33	75	20
9	1–6	33	64	17
Means for all PFs		36	85	21.2
SDs for all PFs		16	36	14.5

characteristics. We developed procedures and software to visualize and analyze the local shapes of individual PFs (Figure 3 and Supplemental Data, Part 3). Coordinates along each PF were extracted as X,Y values in the plane of the PF, and multiple PFs were displayed in a single frame of reference. Figure 3A compares PFs from MTs in vitro (Mandelkow et al., 1991) with non-KMTs and KMTs from PtK₁ cells in mitosis. Most PFs in vivo have shapes that are intermediate between the PFs of P- and D-MTs. To quantify local PF curvature, we fit a circle to each region along the PF and took the reciprocal of its radius (Figure 3B, box). The distributions of mean local PF curvature for MTs in vivo also lie between the comparable values of P- and D-MTs, confirming the differences between these populations (Figure 3B, graph).

Given the diversity in local PF shape, we sought new measures that would allow statistically meaningful comparisons between PFs from different MT groups. The angle between a line perpendicular to the MT axis and the PF segment 6–12 nm from the MT wall was chosen as a good descriptor (Figure 3C, box) because this was the place nearest to the MT wall that showed clear differences between P- and D-MTs. With this metric the distribution of PF orientations on D-MTs showed a peak at relatively small angles (26°–34°), as expected for highly curved PFs (Figure 3C, graph). The PFs of P-MTs were predominately straight, so an angle of ~90° was common, but there were also two small peaks: one at ~72°, which corresponded to the gently curving

PFs, and one at ~26°, which resembled D-MTs. The latter may represent PFs that were depolymerizing at the instant of freezing.

We used these orientations to sort PFs objectively into four distinct groups (Figure 3D). Two groups ("short & blunt" PFs with orientations ~90° and "extensions," 72°–90°) comprise ~90% of the PFs on P-MTs. It is therefore plausible that PFs with this shape in vivo (21% of the PFs on KMTs and 29% on non-KMTs) were polymerizing at the time of freezing. A third group, called "ram's horns" (orientation < 40°), is likely to reflect depolymerization because ~70% of the PFs on D-MTs in vitro had this orientation. Only 29% of the PFs on KMTs and 40% of those on non-KMTs had these angles. The remaining "intermediate" group (orientations from 40° to 72°) included 17% of PFs from D-MTs and none from P-MTs, but it contained 30% of the PFs from non-KMTs and ~50% from KMTs (Figures 3C and 3D). These representations demonstrate that the intracellular environment modifies the structure of many MTs ends so that their PFs differ from those in vitro. Moreover, there are measurable differences between PFs on KMTs and those on non-KMTs.

Treating KMT and non-KMT PFs as classes provided sufficient numbers to permit statistically meaningful distinctions, but it obviated consideration of MTs as individuals. It would have been useful to characterize each MT as polymerizing, depolymerizing, or in some other state, but when we used the objectively sorted PFs to try to classify individual MTs, the results only confirmed the variability of PF shape (Supplemental Text).

Differences between PF Shapes In Vivo and In Vitro Are Not due to Variation in PF Adhesion

The results from looking at PFs by MT class motivated a quest for factors that might make PFs in living cells different from those in vitro. The distribution of D-MT PFs displayed a shoulder containing ~17% of this class (Figure 3C, graph); these PFs comprised a group whose local curvatures grew more slowly than the rest (group 2 on Figures 3A and 3E), resulting in intermediate orientations. These MTs were assembled from pure tubulin, so this fraction could not have arisen from MAPs or local environment. After considering several possible explanations (Supplemental Text), we concluded that they probably resulted from a combination of the way the data were collected and a tendency for PFs in vitro to adhere as they begin to flare. It followed that greater PF adhesion in vivo might account for the larger number of intermediate PFs on spindle MTs, but direct examination of this hypothesis has rejected it (Supplemental Text); PF adhesion cannot explain the differences between PF shape in vivo and in vitro.

MT-Associated Proteins Could Account for the Shapes of Non-KMT PFs, but the Factors That Shape KMT PFs Are More Complex

Most spindle MTs bind MAPs, including "tip-interacting proteins" (Morrison, 2007). There are currently only limited data with which to assess the effects of these proteins on PF curvature (Arnal et al., 2004), but it is reasonable to assume that such binding would change local PF curvature consistently throughout its flare. Indeed, the local curvature of non-KMT PFs with intermediate orientation was markedly constant as
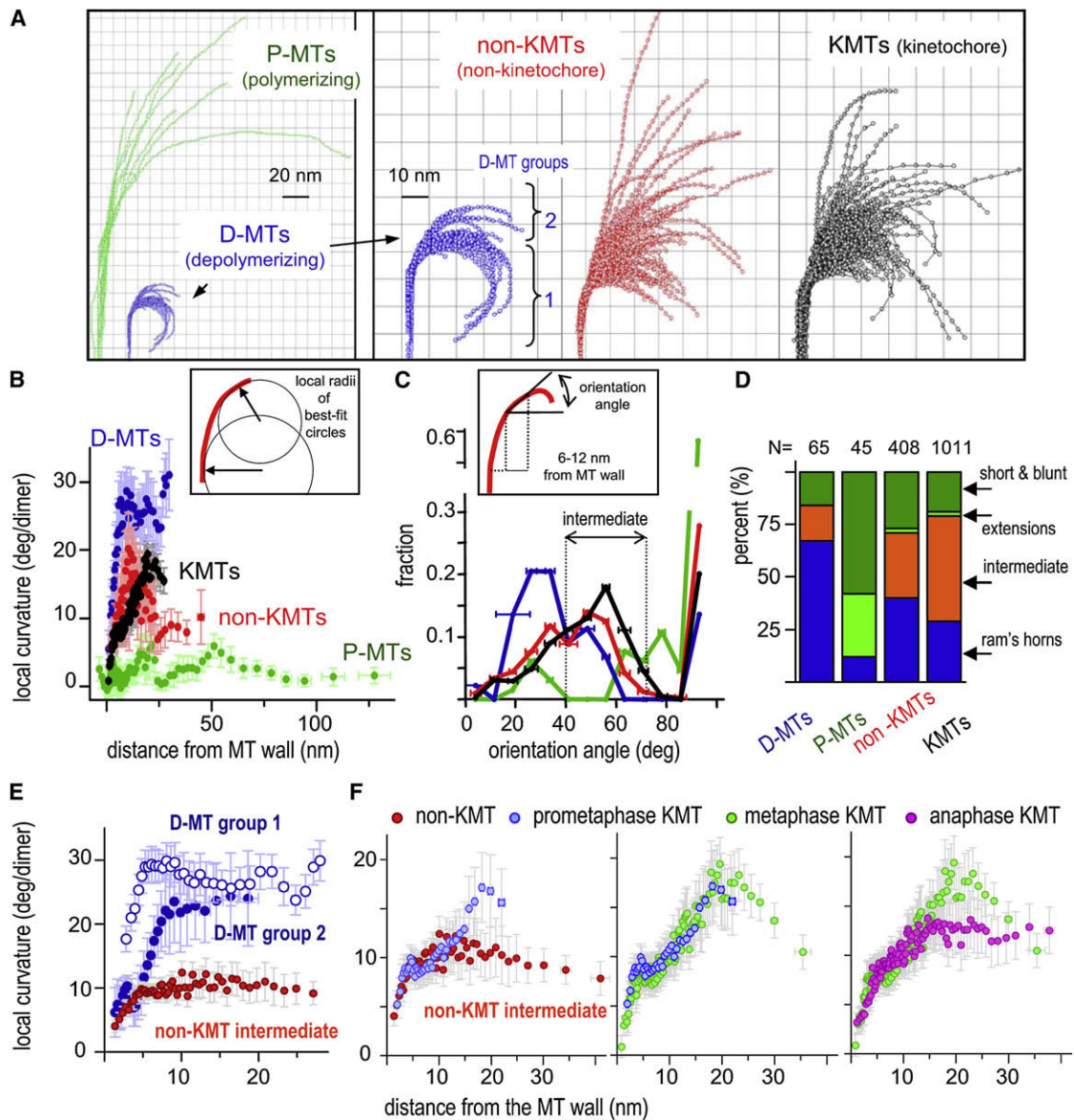
Figure 3. Quantitative Analysis of Local PF Shape

(A) PFs from different MT ends: polymerizing (green) and depolymerizing (blue) MTs formed from pure tubulin in vitro (Mandelkow et al., 1991). Non-KMT PFs (red) are from plus MT ends near the pole of a metaphase PtK$_1$. KMT PFs (black) represented by ~25% of all metaphase and anaphase KMTs, selected at random. Scale for P-MTs is 1/2 that for other MT ends. PFs for D-MTs are shown at both scales for comparison.

(B) Determination and distributions of local curvatures. Box diagrams use of a running average of 10 consecutive points along a PF to determine best-fit circles. Graph displays local curvatures as functions of distance from the MT wall; colors as in (A).

(C) Assessing PF orientation. Box diagrams a strategy for measuring the orientation of PFs in any interval of distances from the MT wall. Graph shows normalized distributions of average PF orientations between 6 and 12 nm from the MT wall for four datasets; colors as in (A). Error bars are SEMs of all PFs in that bin. Most P-PFs are nearly straight, so their greatest fraction is at about 90°, represented with a broken scale.

(D) PFs were sorted into four groups based on their orientation angles (see text). N is the number of PFs in each dataset.

(E) Mean local curvature as a function of distance from MT wall. PFs from D-MTs fall into two groups (panel A). Different local curvature developments as a function of distance from MT wall are consistent with the model that some adjacent PFs adhere close to the wall (group 2).

(F) Mean local curvatures as a function of distance from MT wall for intermediate PFs from metaphase non-KMTs and KMTs from prometaphase, metaphase, and anaphase. The same data for non-KMT PFs are plotted on (E) and (F), for easier comparison.

a function of distance from the MT wall (Figure 3E), consistent with the notion that MAPs bind flaring PFs on these MTs and modify their minimum energy shape.

The local curvature of intermediate PFs from KMTs, however, varied with distance from the MT wall, particularly before anaphase (Figure 3F). Proximal to the MT wall, these PFs were

slightly less curved than those from non-KMTs; farther out, their local curvatures increased, although not to equal that of a D-MT (Figures 3E and 3F). These variations in local curvature suggested that kinetochores provide a special environment that modifies PF structure in complex ways.

PF Shapes Change Little from Metaphase to Anaphase

Unlike previous reports, our analysis of average PF curvature demonstrated changes during the establishment of proper KMT attachment (prometaphase versus metaphase) but not between metaphase and anaphase (Figure 2B). This was surprising, given that metaphase KMTs are, on average, growing at the kinetochore, while anaphase MTs are shortening. We therefore reexamined the issue, looking at local PF structure. The fractions of KMT PFs that resembled P- and D-MTs were very similar in metaphase and anaphase, so we compared the shapes of the intermediate PFs from these stages (Figure 3F). Far from the MT wall, the curvature of anaphase intermediate KMT PFs was both smaller and more constant than that seen in metaphase. Close to the MT wall, however, local PF shapes were very similar. The orientation angles of KMT PFs in metaphase and early anaphase were almost superimposable, but as anaphase proceeded, more PFs with orientations like D-MTs appeared (Figure S2B). Since more MTs are shortening during anaphase than metaphase, the shape of KMT PFs cannot be a simple reflection of dynamic state; other factors must contribute.

The Curvature of KMT PFs Is Low and Constant near the MT Wall, but It Becomes Greater and More Variable Where PFs Encounter Kinetochore-Associated Fibrils

We next examined the vicinity of KMT PFs, seeking structures that might account for their unusual curvatures. A mat of fibers, like that seen by Dong et al. (2007), is visible near the tips of KMTs (Figure S1), but its clarity depends on the thickness of the slices viewed (Figures S1B and S1B′). Our study of PFs was carried out on 2–4 nm slices in which this fibrous mat is subtle (Movie S1), and much of it lies farther from the chromatin than the flared MT end, so it seemed unlikely to account for intermediate PF curvatures. We also sought, but did not find, MT-encircling rings. Flared PFs did, however, frequently associate with fibrils 2–4 nm in diameter; these ran from the PFs to places deeper in the kinetochore (Figure 4A). In our tomographic slices, the material above and below the fibrils was removed from view, so they appeared with good contrast, but their sinuous trajectories made it necessary to step though multiple slices to follow them (Figure 4B). The fibrils were neither robust nor periodic, and their distribution of lengths was broad (Figure 4C). Only in favorable cases was much fibril visible in a single view. Some fibrils linked with straight MT walls, but most connected to flaring PFs. We counted the number of fibrils associated with each PF from 10 KMTs in each of two metaphase and two anaphase cells, a total of 317 PFs: the average fibril/PF ratio was 1.35 ± 0.17; values for metaphase and anaphase were not detectably different. Similar structures were seen on KMTs at all stages of mitosis (e.g., Figures 1B, 1E, and S1), but they were absent from non-KMTs (Figure 1F). We therefore refer to them as kinetochore fibrils (KFs).

To study the relationship between KFs and PF shape, we sorted PFs by their orientation angles, using KMTs and non-KMTs from our two best-preserved metaphase and anaphase cells. Fifty-two of the ninety-eight KMT PFs from a metaphase cell fell in the intermediate class (Figure 4D). Their initial segments were rather straight and made modest angles with the MT axis, but farther from the MT wall the variations in PF curvature grew large (Figure 4E). To ask if these PFs were associated with any specific structures we aligned their images to achieve maximum overlap in their straight and consistently curving parts, then averaged them to reveal any additional consistent features (Figure 4F). The straight and consistently curving parts of the PFs generated good contrast, but the more distal PF parts looked diffuse, as expected. Average images of the intermediate PFs from both metaphase and anaphase KMTs showed a KF extending from near the tip of the well-aligned part of the PF toward the chromatin. No clear KFs were seen in the vicinity of non-KMTs or KMTs from the ram's horn groups, suggesting that KFs with well-defined positions and orientations are specific to KMT PFs with intermediate shape. These results led us to hypothesize that the shapes of intermediate PFs result from interplay between the tendency of GDP-tubulin to curve and forces exerted by KFs that opposed this bending. Such interactions would straighten the PF segments near the MT wall but leave the more distal PF parts in diverse configurations. The reaction to this force would be a poleward pull on the inner kinetochore, potentially accounting for the ability of MT depolymerization to move chromosomes.

Bending PFs Can Act through KFs to Generate Processive and Efficient Chromosome Movement

To ask whether a KF could in principle couple MT depolymerization to chromosome movement, we used our molecular-mechanical model for depolymerizing MTs (Molodtsov et al., 2005), modified to include elastic elements (KFs) that connected the tubulin in flaring PFs to "cargo" (e.g., a chromatid) (Supplemental Data, Part 2). Briefly, each PF is modeled as a linear array of tubulins that interact with defined energy relationships. KFs are assumed to bind at random places along the PF but not to soluble tubulin. As PFs tend toward their minimum energy conformation (~23° bend/dimer), a bound KF opposes this tendency. When tubulin depolymerizes from the tip of a bending PF, any associated KF is released and joins the pool of fibrils that interact randomly with KF binding sites. We examined the role that such fibrils might play in chromosome motion by varying the KF-tubulin association constant (parameter k_+ in Supplemental Data, Part 2). If binding was weak ($k_+ < 25$ s^{-1}), only a few of the MT's 13 PFs bound KFs at any time. As the PFs curled, they pulled on the bound KFs; PFs that failed to form lasting KF connections peeled away from their load, so it stalled (Movie S5 and Figure S3A). When PF-KF binding was stronger ($k_+ > 50$ s^{-1}), cargo moved steadily, driven by PF power strokes (Movie S6). Thus, fibrous connections to bending PFs can theoretically couple MT depolymerization to processive cargo motion, even against a significant load. In fact, fibrillar coupling can move a larger load than can be moved by rings formed by Dam1 complexes, which are thought to perform this function in yeasts (Figure 5A). A ring that binds MTs strongly enough to provide processive coupling impedes
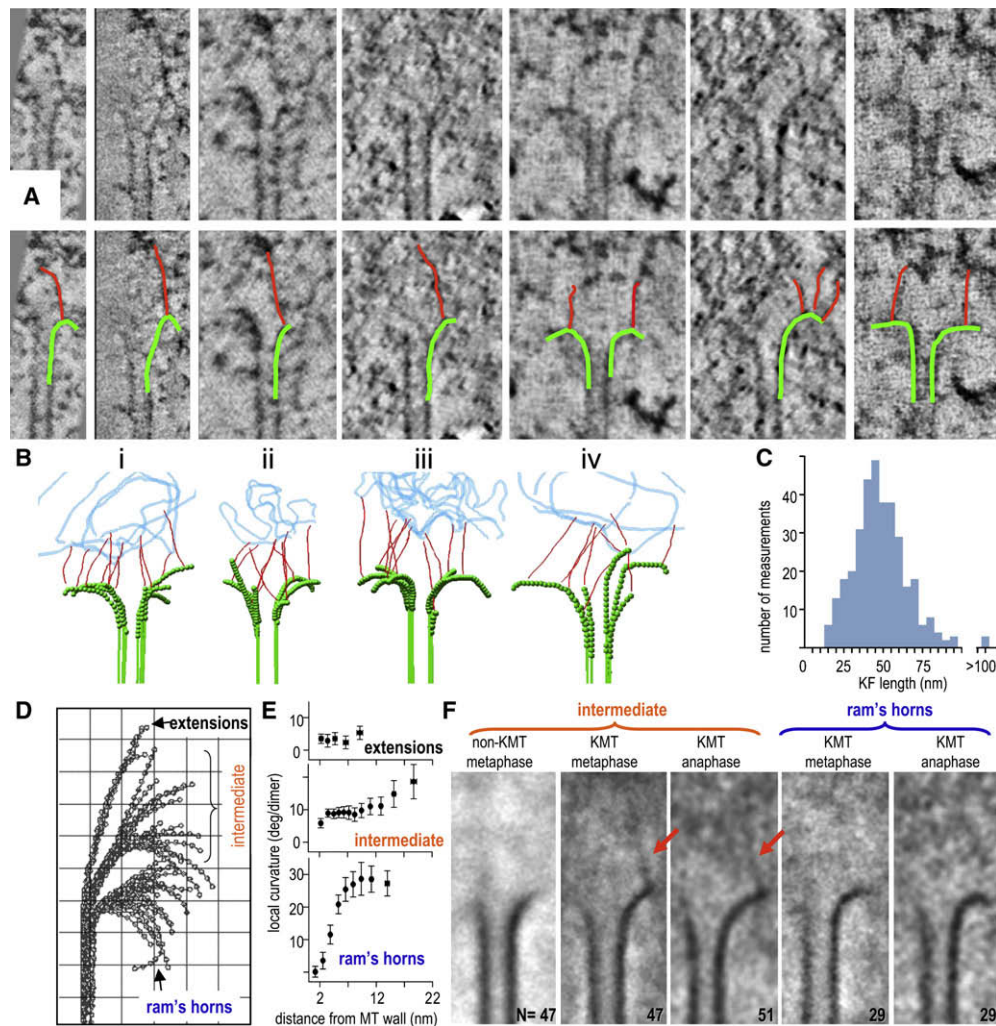
Figure 4. Fibrils Associate with PFs at Places That Correlate with Changes in Local PF Curvature

(A) Tomographic slices of KMT ends. The same gallery is also shown with PFs and their associated KFs indicated by graphic overlays.

(B) Models of metaphase (i, ii) and anaphase (iii, iv) KMT ends; PFs traced in green, KFs in red; a representation of chromatin is in blue.

(C) Histogram of KF lengths based on data from 40 KMTs chosen at random from four cells.

(D and E) PFs from all the KMTs reconstructed by electron tomography from one metaphase kinetochore. PFs were grouped by their orientation angles. Mean local curvatures of each group are plotted in (E). The intermediate group of PFs is conspicuous for its consistent local curvature near the MT wall and its curvature variation farther from the wall. Grid = 10 nm.

(F) Averages of multiple tomographic slices containing PFs from different groups (numbers as indicated). Alignments maximized overlap for the PFs curving right. Intermediate group PFs from metaphase non-KMTs average well, but no KF is evident. Intermediate group KMT PFs from one metaphase and one anaphase cell show 45–54 nm KFs, attached to the averaged PF and extending toward the chromatin. Averages of the ram's horn groups from metaphase and anaphase cells showed no additional electron density at PF tips.

MT shortening and reduces the work that MT depolymerization can accomplish (Grishchuck et al., 2008b). In contrast, KFs undergo cycles of detachment/reattachment, so the efficiency of the depolymerization motor is not limited (Figure 5A and Supplemental Data, Part 2).

The Shapes of Intermediate KMT PFs Could Result from Their Interaction with Fibrils but Not with MT-Encircling Structures

To assess the ability of forces acting through either fibrils or rings to account for structures of KMT PFs, we compared observed PF morphologies with those calculated for PFs under various tensions applied either by randomly attaching KFs or by a MT-encircling ring. Increased tension from KFs straightened the PFs (Figure 5B); the average shape of model PFs experiencing 3–4 pN per PF matched well the average shape of intermediate KMT PFs. Processive movement under this load would result from 1.35 ± 0.15 KFs per PF, a ratio almost identical to that seen in tomograms (above). The theoretical and experimental PFs were also similar in both their gentle and consistent curvature near the MT wall and their more variable behavior in distal regions (Figure 5C).
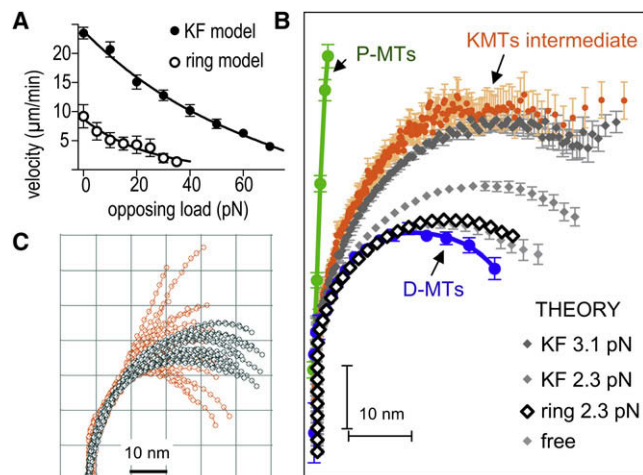
Figure 5. PFs as Mechanical Elements That Can Do Work as They Bend

(A) Force velocity curves for motions of various loads, due to shortening MTs acting through two types of couplers. Data for ring coupler are from Efremov et al. (2007).

(B) Average PF shapes from P-MTs (N = 45) or D-MTs (N = 65) compared with the average shape of intermediate KMT PFs (N = 505). Curves in different grays show theoretical PFs under various tensions applied by randomly attaching KFs. Bars are SEMs. PFs interacting with a Dam1-like ring (diamonds) are experiencing 2.3 pN/PF. Larger forces stall motion and induce ring detachment (A) (Efremov et al., 2007).

(C) Comparison of intermediate PFs from one metaphase kinetochore (orange, same set as Figure 4D) with a family of theoretical PFs (gray) under an average tension of 3.1 pN/PF. The model describes PF straightening close to the MT wall quite well, but the spread in the data farther from the wall indicates the presence of unidentified factors that modify these PF parts.

When the same MT model was used to predict PF shape as tension was applied via a MT-encircling ring, like the Dam1 complex described theoretically in Efremov et al. (2007), the fit to observed PF shape was poor (Figure 5B; Supplemental Data, Part 2). Such rings associate with the MT wall in front of the PF flare, so applied tension has little effect on PF shape, even when it is the maximum that the ring can withstand. This suggested that rings or other MT-encircling structures are not likely to explain KMT PF shape and may therefore not be involved in coupling PF-generated forces to kinetochores in PtK$_1$ cells.

Fibrillar, Kinetochore-Localized Proteins Can Couple MT Depolymerization to Movement of Beads In Vitro

Some evidence from the literature supports the idea that filamentous proteins might enable processive cargo motion at the ends of depolymerizing MTs. Chromosomes will move with MT depolymerization in vitro when soluble nucleotide is <1 nM (Coue et al., 1991), but domain-specific antibodies to the neck of CENP-E (a kinetochore-associated kinesin) block this motion (Lombillo et al., 1995a). Recent work on the structure of CENP-E has shown that a highly flexible, ~200 nm coiled-coil separates the MT-binding and kinetochore-binding domains of this protein (Kim et al., 2008), reminiscent of the longest KFs seen here. This fibrous, processive, plus-end-directed motor may therefore

couple kinetochores to MTs in ways that contribute to minus-end-directed motion with the ends of shortening MTs.

Another candidate for fibrous coupling is the ~57 nm long, 4-subunit Ndc80 complex (Hec1), which is both highly conserved and essential for kinetochore-MT interactions in many cell types (Davis and Wordeman, 2007). Recent work has reconstituted the Ndc80 complex from *C. elegans* in vitro (Cheeseman et al., 2006), so we asked whether it could support the motion of microbeads with depolymerizing MTs. Beads coated with Ndc80 bound readily to MTs (Figure 6A). When MT depolymerization was induced, most beads detached, but ~10% moved toward the minus MT ends (N = 211). The mean distance traveled was 2.1 μm, so these motions were not very processive, although a few beads moved as much as 9 μm (Figures 6B and 6C; Movie S7). The probability that these motions were random is <0.05 (Figure S4). Their average speed was 18 ± 3 μm/min, about the same as the rate of MT shortening in our system. Together with the CENP-E data cited above, the behavior of this fibrous protein complex shows that cargos can be coupled to MT depolymerization by a ring-independent mechanism, although it remains to be seen whether their movement is like that predicted in Movie S6. Thus, the structure of the kinetochore-MT interface, a rigorous theory of depolymerization-dependent motion, and experiments with appropriately shaped proteins all support the idea that fibrous coupling may be important in chromosome motion.

DISCUSSION

Our methods for visualizing and analyzing PFs have demonstrated structural differences between the ends of MTs in vivo and in vitro, and they have drawn particular attention to the complexity of the PFs on KMTs.

Our Data Extend Published Evidence on the Structure of Chromosome-MT Coupling

Previous studies of kinetochores from vertebrate cells have emphasized an outer plate that surrounds KMTs and appears attached to chromatin (reviewed in Rieder and Salmon, 1998 and exemplified by Dong et al., 2007). Our tomographic slices of rapidly frozen, freeze-substitution fixed mitotic PtK$_1$ cells confirm the existence of a fibrillar mat at the outer kinetochore (Figures 1 and S1 and Movie S1), but its clarity depends on mitotic stage and the thickness of the slice being viewed. Our images instead have emphasized slender fibrils (KFs) that connect MT ends with a deeper region of the kinetochore. KFs have not previously been reported, perhaps because of differences between our methods for specimen and image preparation and those used in published work (Supplemental Text). More likely to be significant, however, was our interest in links between KMTs and chromosomes, rather than an overall description of the kinetochore.

Kinetochore Composition Identifies Many Candidates for Chromosome-MT Coupling

Several kinetochore-MT attachment factors have been identified; these protein complexes come in at least two shapes: rings and fibers (Davis and Wordeman, 2007). The Dam1/DASH
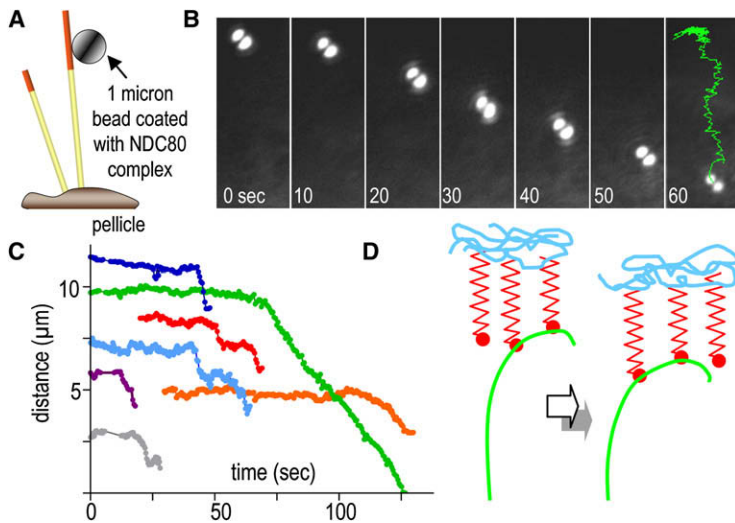
Figure 6. Beads Coated with Ndc80 Complex Move with Depolymerizing MTs In Vitro

(A) Experimental design (not to scale). Bovine brain MTs were capped with GMPCPP-assembled, rhodamine-labeled tubulin, so they would uncap upon illumination with green light, permitting MT depolymerization.

(B) Bead position at times shown (sec); last time shows trajectory of bead center for the entire motion.

(C) Distances from bead to pellicle as a function of time for seven separate experiments. Movement began shortly after the MT cap was removed.

(D) Two consecutive times during the life of a PF from a depolymerizing MT that is stably attached to a load. The propagation of depolymerization, reflected in a progression of PF position, allows recycling KFs to transmit force to the load without a noticeable change in PF curvature where the KFs attach.

complex, which oligomerizes to form rings around MTs in vitro (Miranda et al., 2005; Westermann et al., 2005, 2006), is required for proper chromosome segregation in budding yeast (Cheeseman et al., 2002); it also works as a processive coupler in vitro (Asbury et al., 2006; Grishchuk et al., 2008a). In fission yeast, however, an homologous complex is not essential for normal spindle function (Gachet et al., 2008; Sanchez-Perez et al., 2005), and close Dam1 homologs have not yet been found in other organisms. These results point to other MT-associated, kinetochore-localized proteins, like EB1, XMAP215, Clip 170, CLASP, INCENP, CENP-E, CENP-F, KNL1, and Ndc80/Hec1, all of which have been implicated in MT-kinetochore attachment and/or the regulation of KMT dynamics (reviewed in Morrison, 2007). Of these, CENP-E, XMAP215, and the Ndc80 complex are filamentous, CENP-F and KNL1 are likely to be, and other proteins may associate to make fibers. We hope that our evidence for fibrous couplers will draw attention to this shape and encourage structural work on all these candidate couplers.

The Ndc80 complex is a particularly interesting member of this group because it is both ubiquitous and essential for kinetochore-MT interaction (DeLuca et al., 2006; McAinsh et al., 2006). It is, however, too short to account for all the KFs seen, and its demonstrated binding is to the MT wall, not the polymer's end. Our structural evidence suggests that KFs may bind PFs on a portion of the tubulin dimer that normally faces the MT lumen, a region not commonly explored in MT-binding studies. The resolution of our images is not sufficient to say exactly where KFs and PFs meet, so this question deserves further study.

KMT End Structure Emphasizes the Importance of Fibrils, but Rings Too May Be Important

Our analyses of ring-shaped and fibrillar couplings (Figure 5) suggest that fibrils account better than rings for PF structure at the kinetochore-MT interface. Although rings have not yet been seen on KMTs in vivo, they may still be present and important for some aspect of mitosis. They may contribute to chromosome-MT coupling in some organisms, and they may regulate MT dynamics (Grishchuk et al., 2008b), a critical issue when there is only one MT per kinetochore, as in budding yeast. The

MT-encircling fibrous mat in some kinetochores may also work as a polymerization regulator, keeping the dynamics of multiple KMTs in harmony so that they can all function effectively for kinetochore motion. As shown above and in the Supplemental Data, however, fibrils offer advantages of efficiency when multiple MTs are available to effect reliable chromosome segregation (Figure 5A).

PF-KF Binding Explains Aspects of Spindle Physiology

It has been proposed that inhibiting PF bending slows MT shortening (Franck et al., 2007; Grishchuk et al., 2005; McIntosh et al., 2002). If PFs are prevented from bending by KF tension, for example, when a KF is attached to a metaphase kinetochore whose sister is being pulled toward the opposite pole, then the rate at which KMTs lose tubulin will be reduced. This explains both the intermediate curvature of metaphase KMT PFs and the greater stability of KMTs relative to non-KMTs. It can also rationalize aspects of KMTs "flux," i.e., their slow, poleward movement while kinetochores are on average at rest (Ganem and Compton, 2006). Flux requires that KMTs add subunits at their plus ends in spite of PF flare. We propose that KMT plus-end structure reflects a steady state in which KFs inhibit PFs from attaining the curvature at which depolymerization becomes rapid. The shortening of such MTs is continuously being rescued, so polymerization can continue, even though most PFs are flared.

Some details of PF shape change during mitosis are also rationalized by the idea that KF tension modifies PF curvature. Both the length and average curvature of PFs change as proper chromosome attachments are formed during prometaphase; this may reflect increased tension at sister kinetochores as chromosome attachments mature. However, average PF structure changes little with anaphase onset. Metaphase chromatids are obviously under tension, but many early anaphase chromosomes may likewise experience drag from their sisters as chromatid arms disengage. Kinetochores at both stages may therefore be pulling a considerable load. By mid-anaphase, however, the force necessary for chromosome movement should be reduced to viscous drag and action against any "governor" that

regulates chromosome speed. This may explain why PF orientation is different in early and mid-anaphase and why PF curvature in anaphase is relatively constant as a function of distance from the MT wall (Figure 3B).

A PF with constant curvature can exert a processive force, thanks to the ability of KFs to detach as tubulin depolymerizes and recycle to PF regions nearer the MT wall (Figure 6D). Our results do suggest, however, that the tension developed by PF bending is rather high, and it is not yet clear why this force does not cause chromosomes to move faster. Perhaps, as suggested above, other kinetochore complexes, like Dam1 rings or the outer kinetochore mat, are governors that regulate the rate at which PFs can bend as chromosomes move. Then tension would not be rate limiting unless load became large, e.g., from a persistent connection between sisters.

EXPERIMENTAL PROCEDURES

Cell Culture

PtK$_1$ cells were grown by standard methods and plated on either chips of plastic or PET track-etched membranes (Morphew and McIntosh, 2003). When ~80% confluent, cells were cryo-immobilized in an HPM-010 high-pressure freezer (Bal-Tec AG, Liechtenstein) then fixed by freeze-substitution at $-90°C$ in acetone containing glutaraldehyde and tannic acid, then OsO$_4$ and uranyl acetate; embedding was in Epon-Araldite. The reliability of these methods was tested by comparison with alternative methods (Supplemental Data, Part 1; Tables S3 versus S4, S5 versus S6).

Microtomy, Microscopy, and 3D Reconstruction

Samples were serially sectioned on an UltraCut microtome (Leica Microsystems, Vienna). Sections were picked up on "slot" grids with a 1 × 2 mm hole covered by Formvar, then post-stained in 2% uranyl acetate and lead citrate for 15 and 3 min, respectively. Cellular regions were selected and imaged with either a JEM-1000 (Japanese Electron Optical Laboratories, Tokyo, JP) or an F-30 (FEI Co., Einhoven, NL), using Gatan CCD cameras to record serial tilts from ± 60° or 70° in increments of 1°–1.5°. Each section was imaged in 2 tilt series around orthogonal axes, then assembled into a single reconstruction (Mastronarde, 1997).

Acquiring Images of MT Ends

Spindle MTs were traced, and ends that lay within the reconstructed volume were studied further. Special purpose programs (*mtrotlong* and *rotallends* from IMOD; Kremer et al., 1996) were used to find and excise rectangular solids, ~140 × 120 × 300 nm, that included the plus end of each MT and the region around it. The Slicer feature of IMOD was then used to examine this volume by making its axis of rotation parallel to the excised MT, adjusting the thickness of the displayed slice to 4 nm, and then tipping the orientation of the slice to angles as high as ± 60°. We searched a range of tilts to find an orientation that displayed one or more clearly curling PFs. The two MT walls and any flaring PFs were then traced by hand, a process that involved some judgment. For example, any place along a possible PF that showed a sharp change in curvature (e.g., 90° in a few pixels) or an obvious change in thickness or stain density was interpreted as the association of that PF with some other object, not a continuation of the PF.

After two PF traces on one MT end had been stored, the orientation of the sampling plane was changed by 28° ± 6° to find additional PFs on the same MT (360°/13 = 27.7; ± 6° allows for variation, given the distortions of plastic sections). Most MT ends yielded six satisfactory PF tracings.

Quantitative Structural Characterization of Microtubule Ends

The average structure of each PF trace was assessed by the *howflared* program in IMOD. This returns a table of numbers that describe the average path of the PF from the point it diverged from the MT wall to its end. The average curvature of each PF was expressed as the average angle between adjacent 8 nm segments, i.e., degrees/dimer. To examine variation along a PF, we used the two-dimensional (2D) coordinates of each PF, mapped to a single frame of reference that allowed both sorting by shape and quantification of local curvature as a function of distance from the MT wall, using the "Curvature Calculation Program" (Figures 4 and S5 and Supplemental Data, Part 3). This software was also used to compute PF orientation angles and to calculate the mean local curvatures of each PF group.

To create average images of the PFs and their surroundings, we used Metamorph 6.4 (Universal Imaging) to align all images of a given PF class so that there was maximal overlap in the straight and consistently curving parts of the PFs. The aligned images were averaged then contrasted using PhotoShop.

Mathematical Model of Fibrillar Coupler

Calculations were carried out using the Monte Carlo-Metropolis method (Heermann, 1990). A detailed description of our model of KFs interacting with bending PFs is given in Supplemental Data, Part 2. Briefly, each PF bending was modeled as described in Molodtsov et al. (2005) and modified in Efremov et al. (2007). The kinetochore was modeled as a plane disk that could move along a MT axis. On its MT-proximal surface the disk bound one fibril per 200 nm^2, a total of ~50; the opposite surface of the kinetochore was connected to various "loads," so we could examine the load-velocity relationship for this coupler. KFs were modeled as flexible, elastic elements 80 nm long that attached strongly (no exchange) at the kinetochore disk. The kinetochore-distal end of each fibril had a specific tubulin-binding site, one per polymerized tubulin dimer, although models that assumed one binding site per monomer produced similar results. KF-MT association was modeled with an on-rate only because the off-rate was assumed to be negligible until tubulin depolymerized, whereupon it became high, releasing the KF to recycle and bind any other KF-binding site on the still-polymerized tubulin. During our analysis of this model, we varied the physical characteristics of both the KFs and the PFs over considerable ranges of plausible values, seeking any singularities or unexpected features of the model (Supplemental Data, Part 2). These calculations showed that the proposed coupling mechanism is robust to considerable variation, so long as the binding of the KFs to the PFs is strong.

In Vitro Assay of MT-Depolymerization-Dependent Motility

Bead motility was examined as described in Grishchuk et al. (2008a). Briefly, MTs were grown from coverslip-attached *Tetrahymena* pellicles, using purified bovine brain tubulin. MT ends were stabilized with rhodamine-labeled tubulin, assembled with GMPCPP, so depolymerization could be induced by photo-dissolution of the caps. *C. elegans* Ndc80 complex was purified as described (Cheeseman et al., 2006). Polystyrene 1μm beads coated with streptavidin (Bangs Laboratories) were incubated with biotinylated pentaHIS-antibodies (QIAGEN), followed by the Ndc80 complex, in which the Spc24 subunit was tagged with 6HIS. Successful conjugation was confirmed with anti-Ndc80 antibodies. The conjugation density was ~5 × 10^4 Ndc80 complexes per bead, enough for up to 40 fibrils to contact one MT end. Images were acquired and analyzed using Metamorph.

SUPPLEMENTAL DATA

Supplemental Data include Supplemental Text, nine tables, five figures, and seven movies and can be found with this article online at http://www.cell.com/cgi/content/full/135/2/322/DC1/.

REFERENCES

Arnal, I., Heichette, C., Diamantopoulos, G.S., and Chretien, D. (2004). CLIP-170/tubulin-curved oligomers coassemble at microtubule ends and promote rescues. Curr. Biol. *14*, 2086–2095.

Asbury, C.L., Gestaut, D.R., Powers, A.F., Franck, A.D., and Davis, T.N. (2006). The Dam1 kinetochore complex harnesses microtubule dynamics to produce force and movement. Proc. Natl. Acad. Sci. USA *103*, 9873–9878.

Cheeseman, I.M., and Desai, A. (2008). Molecular architecture of the kinetochore-microtubule interface. Nat. Rev. Mol. Cell Biol. *9*, 33–46.

Cheeseman, I.M., Drubin, D.G., and Barnes, G. (2002). Simple centromere, complex kinetochore: linking spindle microtubules and centromeric DNA in budding yeast. J. Cell Biol. *157*, 199–203.

Cheeseman, I.M., Chappie, J.S., Wilson-Kubalek, E.M., and Desai, A. (2006). The conserved KMN network constitutes the core microtubule-binding site of the kinetochore. Cell *127*, 983–997.

Chretien, D., Fuller, S.D., and Karsenti, E. (1995). Structure of growing microtubule ends: two-dimensional sheets close into tubes at variable rates. J. Cell Biol. *129*, 1311–1328.

Coue, M., Lombillo, V.A., and McIntosh, J.R. (1991). Microtubule depolymerization promotes particle and chromosome movement in vitro. J. Cell Biol. *112*, 1165–1175.

Davis, T.N., and Wordeman, L. (2007). Rings, bracelets, sleeves, and chevrons: new structures of kinetochore proteins. Trends Cell Biol. *17*, 377–382.

DeLuca, J.G., Gall, W.E., Ciferri, C., Cimini, D., Musacchio, A., and Salmon, E.D. (2006). Kinetochore microtubule dynamics and attachment stability are regulated by Hec1. Cell *127*, 969–982.

Dong, Y., Vanden Beldt, K.J., Meng, X., Khodjakov, A., and McEwen, B.F. (2007). The outer plate in vertebrate kinetochores is a flexible network with multiple microtubule interactions. Nat. Cell Biol. *9*, 516–522.

Efremov, A., Grishchuk, E.L., McIntosh, J.R., and Ataullakhanov, F.I. (2007). In search of an optimal ring to couple microtubule depolymerization to processive chromosome motions. Proc. Natl. Acad. Sci. USA *104*, 19017–19022.

Franck, A.D., Powers, A.F., Gestaut, D.R., Gonen, T., Davis, T.N., and Asbury, C.L. (2007). Tension applied through the Dam1 complex promotes microtubule elongation providing a direct mechanism for length control in mitosis. Nat. Cell Biol. *9*, 832–837.

Gachet, Y., Reyes, C., Courtheoux, T., Goldstone, S., Gay, G., Serrurier, C., and Tournier, S. (2008). Sister kinetochore recapture in fission yeast occurs by two distinct mechanisms, both requiring dam1 and klp2. Mol. Biol. Cell *19*, 1646–1662.

Ganem, N.J., and Compton, D.A. (2006). Functional roles of poleward microtubule flux during mitosis. Cell Cycle *5*, 481–485.

Grishchuk, E.L., and McIntosh, J.R. (2006). Microtubule depolymerization can drive poleward chromosome motion in fission yeast. EMBO J. *25*, 4888–4896.

Grishchuk, E.L., Molodtsov, M.I., Ataullakhanov, F.I., and McIntosh, J.R. (2005). Force production by disassembling microtubules. Nature *438*, 384–388.

Grishchuk, E.L., Spiridonov, I.S., Volkov, V.A., Efremov, A., Westermann, S., Drubin, D., Barnes, G., Ataullakhanov, F.I., and McIntosh, J.R. (2008a). Different assemblies of the DAM1 complex follow shortening microtubules by distinct mechanisms. Proc. Natl. Acad. Sci. USA *105*, 6918–6923.

Grishchuk, E.L., Efremov, A.K., Volkov, V.A., Spiridonov, I.S., Gudimchuk, N., Westermann, S., Drubin, D., Barnes, G., McIntosh, J.R., and Ataullakhanov, F.I. (2008b). The Dam1 ring binds microtubules strongly enough to be a processive as well as energy-efficient coupler for chromosome motion. Proc. Natl. Acad. Sci. USA. Published online September 29, 2008. 10.1073/pnas.0807859105.

Heermann, D.W. (1990). Computer Simulation Methods in Theoretical Physics (New York: Springer-Verlag).

Hill, T.L. (1985). Theoretical problems related to the attachment of microtubules to kinetochores. Proc. Natl. Acad. Sci. USA *82*, 4404–4408.

Joglekar, A.P., Bouck, D., Finley, K., Liu, X., Wan, Y., Berman, J., He, X., Salmon, E.D., and Bloom, K.S. (2008). Molecular architecture of the kinetochore-microtubule attachment site is conserved between point and regional centromeres. J. Cell Biol. *181*, 587–594.

Kim, Y., Heuser, J.E., Waterman, C.M., and Cleveland, D.W. (2008). CENP-E combines a slow, processive motor and a flexible coiled coil to produce an essential motile kinetochore tether. J. Cell Biol. *181*, 411–419.

Koshland, D.E., Mitchison, T.J., and Kirschner, M.W. (1988). Polewards chromosome movement driven by microtubule depolymerization in vitro. Nature *331*, 499–504.

Kremer, J.R., Mastronarde, D.N., and McIntosh, J.R. (1996). Computer visualization of three-dimensional image data using IMOD. J. Struct. Biol. *116*, 71–76.

Liu, S.T., Rattner, J.B., Jablonski, S.A., and Yen, T.J. (2006). Mapping the assembly pathways that specify formation of the trilaminar kinetochore plates in human cells. J. Cell Biol. *175*, 41–53.

Lombillo, V.A., Nislow, C., Yen, T.J., Gelfand, V.I., and McIntosh, J.R. (1995a). Antibodies to the kinesin motor domain and CENP-E inhibit microtubule depolymerization-dependent motion of chromosomes in vitro. J. Cell Biol. *128*, 107–115.

Lombillo, V.A., Stewart, R.J., and McIntosh, J.R. (1995b). Minus-end-directed motion of kinesin-coated microspheres driven by microtubule depolymerization. Nature *373*, 161–164.

Mandelkow, E.M., Mandelkow, E., and Milligan, R.A. (1991). Microtubule dynamics and microtubule caps: a time-resolved cryo-electron microscopy study. J. Cell Biol. *114*, 977–991.

Mastronarde, D.N. (1997). Dual-axis tomography: an approach with alignment methods that preserve resolution. J. Struct. Biol. *120*, 343–352.

McAinsh, A.D., Meraldi, P., Draviam, V.M., Toso, A., and Sorger, P.K. (2006). The human kinetochore proteins Nnf1R and Mcm21R are required for accurate chromosome segregation. EMBO J. *25*, 4033–4049.

McIntosh, J.R., Grishchuk, E.L., and West, R.R. (2002). Chromosome-microtubule interactions during mitosis. Annu. Rev. Cell Dev. Biol. *18*, 193–219.

Miranda, J.J., De Wulf, P., Sorger, P.K., and Harrison, S.C. (2005). The yeast DASH complex forms closed rings on microtubules. Nat. Struct. Mol. Biol. *12*, 138–143.

Molodtsov, M.I., Grishchuk, E.L., Efremov, A.K., McIntosh, J.R., and Ataullakhanov, F.I. (2005). Force production by depolymerizing microtubules: a theoretical study. Proc. Natl. Acad. Sci. USA *102*, 4353–4358.

Morphew, M.K., and McIntosh, J.R. (2003). The use of filter membranes for high-pressure freezing of cell monolayers. J. Microsc. *212*, 21–25.

Morrison, E.E. (2007). Action and interactions at microtubule ends. Cell. Mol. Life Sci. *64*, 307–317.

Muller-Reichert, T., Chretien, D., Severin, F., and Hyman, A.A. (1998). Structural changes at microtubule ends accompanying GTP hydrolysis: information from a slowly hydrolyzable analogue of GTP, guanylyl (alpha,beta)methylenediphosphonate. Proc. Natl. Acad. Sci. USA *95*, 3661–3666.

O'Toole, E.T., Winey, M., and McIntosh, J.R. (1999). High-voltage electron tomography of spindle pole bodies and early mitotic spindles in the yeast Saccharomyces cerevisiae. Mol. Biol. Cell *10*, 2017–2031.

O'Toole, E.T., McDonald, K.L., Mantler, J., McIntosh, J.R., Hyman, A.A., and Muller-Reichert, T. (2003). Morphologically distinct microtubule ends in the mitotic centrosome of Caenorhabditis elegans. J. Cell Biol. *163*, 451–456.

Rieder, C.L., and Salmon, E.D. (1998). The vertebrate cell kinetochore and its roles during mitosis. Trends Cell Biol. *8*, 310–318.

Sanchez-Perez, I., Renwick, S.J., Crawley, K., Karig, I., Buck, V., Meadows, J.C., Franco-Sanchez, A., Fleig, U., Toda, T., and Millar, J.B. (2005). The DASH complex and Klp5/Klp6 kinesin coordinate bipolar chromosome attachment in fission yeast. EMBO J. *24*, 2931–2943.

Schittenhelm, R.B., Heeger, S., Althoff, F., Walter, A., Heidmann, S., Mechtler, K., and Lehner, C.F. (2007). Spatial organization of a ubiquitous eukaryotic kinetochore protein network in Drosophila chromosomes. Chromosoma *116*, 385–402.

Tanaka, K., Kitamura, E., Kitamura, Y., and Tanaka, T.U. (2007). Molecular mechanisms of microtubule-dependent kinetochore transport toward spindle poles. J. Cell Biol. *178*, 269–281.

VandenBeldt, K.J., Barnard, R.M., Hergert, P.J., Meng, X., Maiato, H., and McEwen, B. (2006). Kinetochores use a novel mechanism for coordinating the dynamics of individual microtubules. Curr. Biol. *16*, 1217–1223.

Wang, H.W., and Nogales, E. (2005). Nucleotide-dependent bending flexibility of tubulin regulates microtubule assembly. Nature *435*, 911–915.

Westermann, S., Avila-Sakar, A., Wang, H.W., Niederstrasser, H., Wong, J., Drubin, D.G., Nogales, E., and Barnes, G. (2005). Formation of a dynamic kinetochore- microtubule interface through assembly of the Dam1 ring complex. Mol. Cell *17*, 277–290.

Westermann, S., Wang, H.W., Avila-Sakar, A., Drubin, D.G., Nogales, E., and Barnes, G. (2006). The Dam1 kinetochore ring complex moves processively on depolymerizing microtubule ends. Nature *440*, 565–569.

Westermann, S., Drubin, D.G., and Barnes, G. (2007). Structures and functions of yeast kinetochore complexes. Annu. Rev. Biochem. *76*, 563–591.

Supplemental Data

Fibrils Connect Microtubule Tips with

Kinetochores: A Mechanism to Couple

Tubulin Dynamics to Chromosome Motion

J.R. McIntosh, E.L. Grishchuk, M. Morphew, A.K. Efremov, K. Zhudenkov, V.A. Volkov, I.M. Cheeseman, A. Desai, D.N. Mastronarde, and F.I. Ataullakhanov

Part 1. *Supplemental Text, Tables, and Figures.*

Supplemental Text

PF flare in vivo is unlikely to be a result of preparative artifact

Both high pressure and cold are well known to depolymerize spindle MTs, so our method for sample preparation might have introduced artifacts. Two kinds of evidence suggest that this is not the case. PFs at the plus ends of chemically fixed KMTs have also been seen to flare (VandenBeldt et al., 2006), and our quantitative methods have found no statistically significant differences between our chemically fixed and high pressure frozen, freeze-substitution fixed metaphase KMTs (compare Tables S3 and S4). We have also assessed PF flare after plunge-freezing, a method that does not employ high-pressure. Mitotic PtK_1 cells are too thick to freeze well by this method, but we obtained one anaphase cell in which detectable freeze damage was limited to the chromatin. KMT flare in this cell was again indistinguishable from that in comparable, high pressure frozen cells (compare Tables S5 and S6). We conclude that there are no effects of high pressure freezing on MT end morphology at a resolution of ~5 nm.

This evidence for reproducibility does not, however, mean that our images are reliable to molecular resolution. All methods for fixation can introduce artifact, so the structural details of both PF curvature and kinetochore-associated fibrils may include minor inaccuracies, e.g., in the shapes of KFs. While the average KF shapes seen in Fig. 4F are quite straight, individual KFs are often sinuous (those shown in Fig. 4A were selected to be particularly evident in a single slice). The straight structure of the average PFs is, however, consistent with the tension we propose that KFs experience in metaphase and early anaphase; the deviations from the average KF structure that are seen with individual KFs is probably a result of thermal fluctuations, fixation artifact, and stain variation, not a great surprise when one realizes the tiny size of the objects in view.

The flare of multiple PFs on individual MTs is highly variable

Examination of all the visible PFs on any one MT end showed that flare was variable; likewise, PFs from all the KMTs from a single kinetochore showed significant variation (Table 1). Further data in support of this statement are presented in Supplementary tables S1 – S8. One might hope that in spite of this variation, the PFs of a single MT would allow one to categorize each polymer as either polymerizing or depolymerizing, based on the extent of flare of all its PFs and analogy with the structures seen in vitro; unfortunately, this is not possible. In Table 1, the (SDs)/(mean values) for length, final angle, and average curvature from the PFs of a single MT are 65%, 54%, and 28%, respectively. Analogous numbers for all the PFs on the 9 MTs shown here from a single kinetochore

(Table 1) are 43%, 42%, and 68%. On a representative set of 13 metaphase KMTs (kfm2s5l), the mean value of the SDs from all the PFs on all the MTs, divided by the means of the average values for the same parameters were 35%, 60%, and 51%. Given the extent of variation demonstrated by these numbers, we concluded that an analysis that treated MTs as individual entities and tried to categorize them by their average flare would be bound to fail. We have therefore grouped all prometaphase PFs, all metaphase PFs, etc., and looked for statistically significant differences between the PFs of one class relative to other classes.

After adopting this grouping strategy, and while we looked for objective ways to categorize PFs, we found that the orientation of each PF a short distance from the MT wall served as an effective discriminator between polymerizing and depolymerizing MTs in vitro (Fig. 3). We therefore asked whether the sorting of PFs by this criterion might allow us to go back more effectively to the problem of categorizing individual spindle MTs into P- or D-MT categories. PF orientation near the MT wall allowed us to put PFs into three categories: "Ram's horns" (orientation $< 40^\circ$, which predominate in depolymerizing MTs in vitro, i.e., D-MTs), "Extensions" and short-blunt PFs (orientation 72° - 90°, which are common in polymerizing MTs, or P-MTs), and "intermediate" PFs, which lie in between.

Using these distinctions we found 30 ram's horn PFs, 0 extension, short-blunt PFs, and 8 intermediate PF in the D-MTs from Mandelkow et al., 1991. Thus, the fraction of ram's horn PFs in this group is 0.67. Among the P-MTs, the same fraction is 0.12. These data imply that MTs that are growing and shortening need not have PFs from only one category, and the behavior of the whole MT will result from the behavior of the majority of its PFs at any one time. Granted, we cannot know for sure that any single MT within a population was either growing or shrinking at the time it was frozen, but the data suggest a cooperative behavior of the PFs on a single MT, based on the structure of the majority. Based on this information it is plausible to say that an in vitro MT with $\geq$ 50% ram's horn PFs is likely to be depolymerizing and vice versa.

We have looked at the fractions of non-KMTs that contain $\geq$ 50% ram's horn PFs in three data sets, and found that it was 1/4. Under the assumption that all these predominantly ram's horn MTs are depolymerizing, the ratio of polymerizing MTs to depolymerizing MTs in this population is about 3:1. This ratio is far from the ratio one would predict from the observed relative rates of MT growing and shortening at steady state in vivo, which are essentially equal in mitotic frog egg extracts (Belmont et al., 1990) and cultured mammalian cells (Rusan et al., 2001). This suggests that plausible criteria for relating MT end morphology to MT dynamic state, developed from MT shape in vitro, are not applicable to MTs in vivo.

One can still ask whether this objective criterion improves on the difficulty, described above, of classifying MTs on the basis of the shapes of all their visible PFs. Unfortunately, it does not. We have been unable to find a criterion that let us categorize PFs individually and then use their predominant behavior on a single MT to categorize the MT's dynamic state. This situation supports our paper's conclusion that the shapes of PFs at the tips of dynamic MTs in vivo are modified by factors that are different from those found in vitro, most notably by tip-associated MAPs and/or interaction with cargo. As a result, there are no current methods to unambiguously identify the polymerization state of a given MT in vivo from the structure of its end.

Differences between PF shapes in vivo and in vitro are not due to variation in PF adhesion

The PFs of D-MTs appear to fall into two groups: one in which the local curvature rises rapidly with distance from the MT wall (Group 1) and another in which it rises more slowly (Group 2) (Fig. 3E). Group 2 PFs might have resulted from the way these data were collected; a single projection image misrepresents the curvature of PFs in planes whose normal is oblique to the microscope axis. Excluding this possibility will require cryo-electron tomography of MTs polymerizing in vitro, a large and important job that has not yet been done. The peak might also derive from PFs that stuck together as they bent away from the MT wall. We tested this hypothesis by quantifying the image darkness of PFs near the MT wall; two adhering PFs should look twice as dark as a single PF. Our results suggest

that as many as 20% of the curved PFs on depolymerizing MTs in vitro might start to flare as complexes of two or more PFs, which may explain the intermediate orientations of Group 2.

If PF adhesion were stronger in vivo than in vitro, the prevalence of "intermediate" PFs in vivo (Fig 3D) would be explained. We tested this idea by examining cellular MT ends with tomographic slices cut at multiple orientations (data like those in Videos 2–4). Among non-KMTs only 2 of 278 PFs appeared to be adhering. Of 216 KMT PFs, < 4% showed evidence of adhesion (Fig S2A). These results eliminate the possibility that increased PF adhesion in vivo, compared with PFs in vitro, is the explanation for the large number of PFs in vivo that show an intermediate curvature.

Technical differences between our methods for sample preparation and imaging, relative to those used in previously published work.

Our description of the structures at the kinetochore-MT interface differs considerably from that in published work, which used similar methods to look at the same cells (Dong et al., 2007; VandenBeldt et al., 2006). There are, however, some technical differences that may account for some of these discrepancies. We imaged the sample with 1 nm pixels, rather than 1.7 nm, giving slightly better image definition, and we employed 300 rather than 200 KeV electrons (less noise from inelastic electron scattering). Our tilt series were acquired with constant tilt increments of 1°, rather than 2° with a cosine modulation of tilt increment, which we find gives better imaging of plastic sections and may have given us better detection of slender structures. We also used thin tomographic slices to study our reconstructions, and we avoided programs that render structural data as surfaces, based on a threshold. These approaches may have let us see and study structures as thin and ephemeral as the PF-associated kinetochore fibrils.

Our visualization of overall kinetochore structure is not, however, much different from the view presented in Dong et al., 2007 and VandenBeldt et al., 2006. We have avoided describing the kinetochore-MT interfacing structure as a "plate" because it is very clear from both published work (Dong et al., 2007) and our own thin tomographic images that this interface is comprised of a dense meshwork of fibrils (KFs and others), rather than a dense plaque with openings for penetrating MTs, as it has commonly been described in reviewing materials.

Finally, we have carried out a quantitative analysis of the structure of flaring PFs, an approach that was absent in previous studies. These differences are likely to explain the discrepancies between our observations and previously published results on the extent of PF flare and the frequency with which PF flare is seen at different mitotic stages.

Supplemental Tables

Average PF structure of MTs in vivo

Tables S1–S8. Average PF parameters as in Table 1 for different numbers (No.) of MTs and their PFs. Data are broken out by stage in mitosis and conditions for sample preparation. Comparisons between the numbers in these tables provide quantitative support for several statements in the paper and the Suppl. Data (see texts for details). The data on average PF length and mean average curvature from different stages of mitosis are also shown in bar graph form in Fig. 2B.

Table S1: Non-KMTs, Metaphase, High-pressure frozen

Cell Name	No. MT	PF Length in nm	Final Angle in degrees	Average Curvature deg/dimer
non-KMT1	41	34.27	59.56	14.88
non-KMT2	22	50.08	88.55	15.92
non-KMT3	22	41.78	90.91	18.24
No. MTs 85	Mean	39.32	72.45	15.68
No. PFs 485	SD	19.44	47.37	9.44

Table S2: Prometaphase, High-pressure frozen

Cell Name	No. MT	PF Length in nm	Final Angle in degrees	Average Curvature deg/dimer
Prometa1	18	36.07	81.87	18.64
Prometa6	12	42.38	68.47	13.38
No. MTs 30	Mean	38.04	77.76	16.96
No PFs 215	SD	13.50	37.90	8.95

Table S3: Metaphase, High-pressure frozen

Cell Name	No. MT	PF Length in nm	Final Angle in degrees	Average Curvature deg/dimer
Kfm1l	18	49.34	54.98	9.72
Kfm1r	12	58.71	66.90	10.08
Kfm2s4l	8	58.99	109.67	15.44
Kfm2s4r	17	50.96	58.77	10.16
Kfm2s5l	13	47.83	76.02	12.64
Kfm2s5r	11	53.08	68.42	10.32
Kfm2s9-1	12	56.85	73.25	10.48
Kfm2s9-2	12	52.91	57.13	8.64
kt1ends1	17	49.43	73.60	11.60
kt1ends2	12	49.45	73.17	12.24
Meta1	22	41.36	69.08	13.28
Meta3	13	40.40	69.81	14.56
Ptk1_2	19	49.49	83.40	13.28
No. MTs 186	Mean	49.46	70.60	11.76
No. PFs 1085	SD	23.01	47.17	7.12

Table S4: Metaphase, Chemically Fixed

Cell Name	No. MT	PF Length in nm	Final Angle in degrees	Average Curvature deg/dimer
Km1l	8	47.16	75.21	13.04
Km1r	7	46.57	60.11	11.28
No. MTs 15	Mean	46.89	68.20	12.24
No. PFs 85	SD	20.33	42.33	2.28

Table S5: Anaphase KMTs, High-pressure frozen

Cell Name	No. MT	PF Length in nm	Final Angle in degrees	Average Curvature deg/dimer
Kfe1-1	21	61.97	90.69	12.08
Kfe1-2	9	43.42	73.45	13.92
Kfe1-3	14	59.34	89.63	12.08
kfma1	16	52.29	64.65	10.88
No. MTs 60	Mean	55.84	80.44	12.08
No. PFs 347	SD	25.47	48.14	6.64

Table S6: Anaphase KMTs, Plunge-frozen

Cell Name	No. MT	PF Length in nm	Final Angle in degrees	Average Curvature deg/dimer
plungeAna	32	50.43	79.08	13.28
No. PFs 193	SD	22.44	42.20	6.40

Table S7: Anaphase KMTs, all data for KMTs

	MTs from S5 & S6	PF Length in nm	Final Angle in degrees	Average Curvature deg/dimer
No. MTs 90	Mean	53.90	79.95	12.48
No PFs 540	SD	24.55	46.07	6.56

Table S8: Anaphase Interpolar MTs

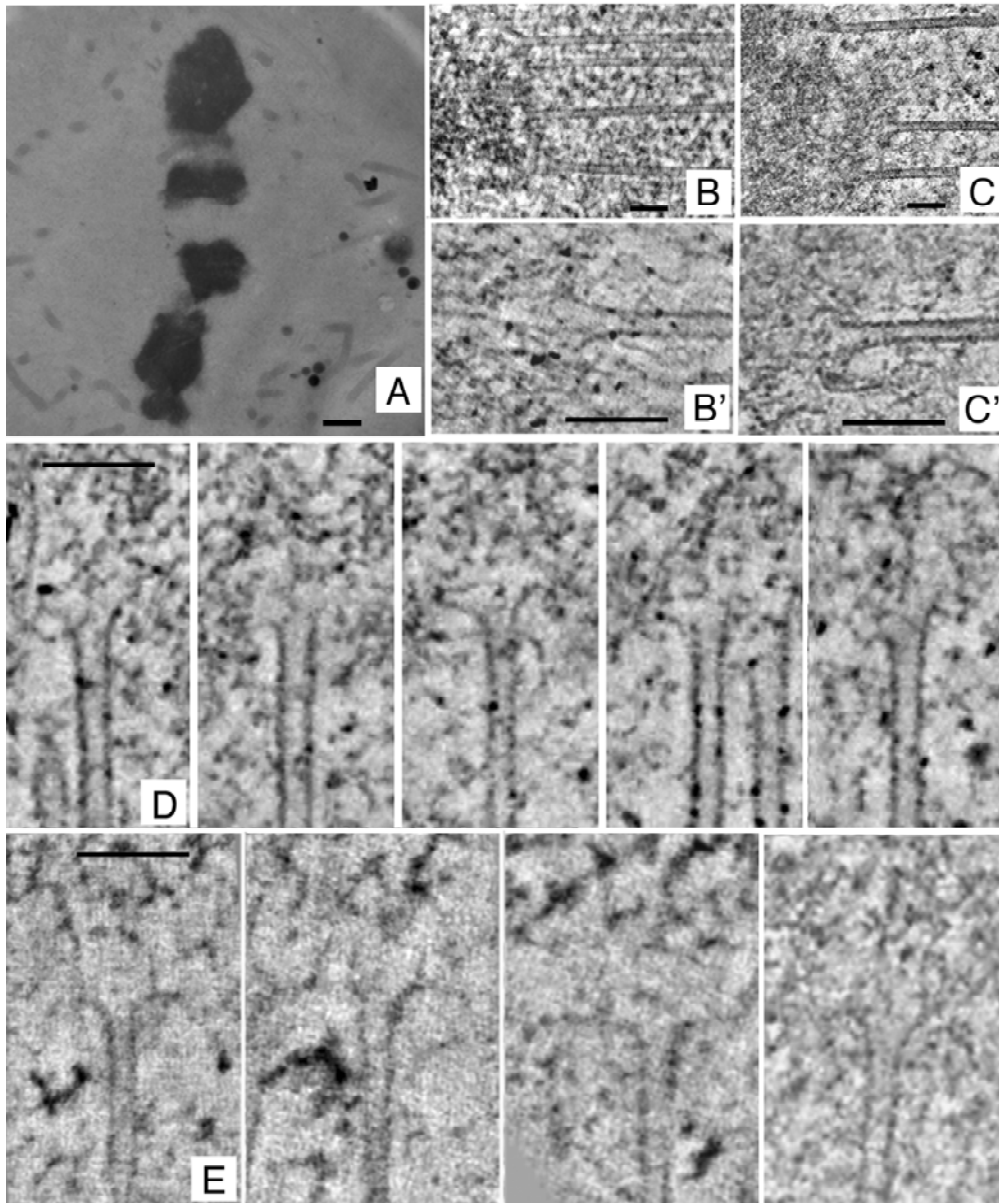| Cell Name	No. MT	PF Length in nm	Final Angle in degrees	Average Curvature deg/dimer
ipmt1	12	47.77	72.15	12.72
ipmt2	17	43.90	83.05	15.04
No. MTs 29	Mean	45.22	79.28	14.24
No. PFs 179	SD	16.22	45.35	6.64

Figure S1. Electron micrographs and tomograms of PtK₁ cells, high pressure frozen and then fixed by freeze-substitution while in metaphase or anaphase. **(A)** A low magnification image of a single 300 nm thick section of the kind used for tomography; the positions of the chromosomes show this to be a metaphase cell. Bar = 1μm. **(B)** An average of 20 tomographic slices, which corresponds to about 40 nm of sample thickness, so the image is similar to an electron micrograph of a conventional thin section. Some plate-like structure is present at the kinetochore when viewed at this thickness. **(B')** A single tomographic slice that shows the MT wall, PF flare, and a few fibrils running from the MT to the chromatin, but a kinetochore plate is very subtle. Bars = 0.1μm. **(C)** and **(C')** Comparable images from a PtK₁ cell in early anaphase. **(D)** A gallery of 5 metaphase KMTs, showing the diversity of PF flare and the structures surrounding these KMT ends. Bar = 0.1μm. **(E)** Four comparable images from a PtK₁ cell in early anaphase. The greater length of some PFs is apparent. Bar = 0.1μm.
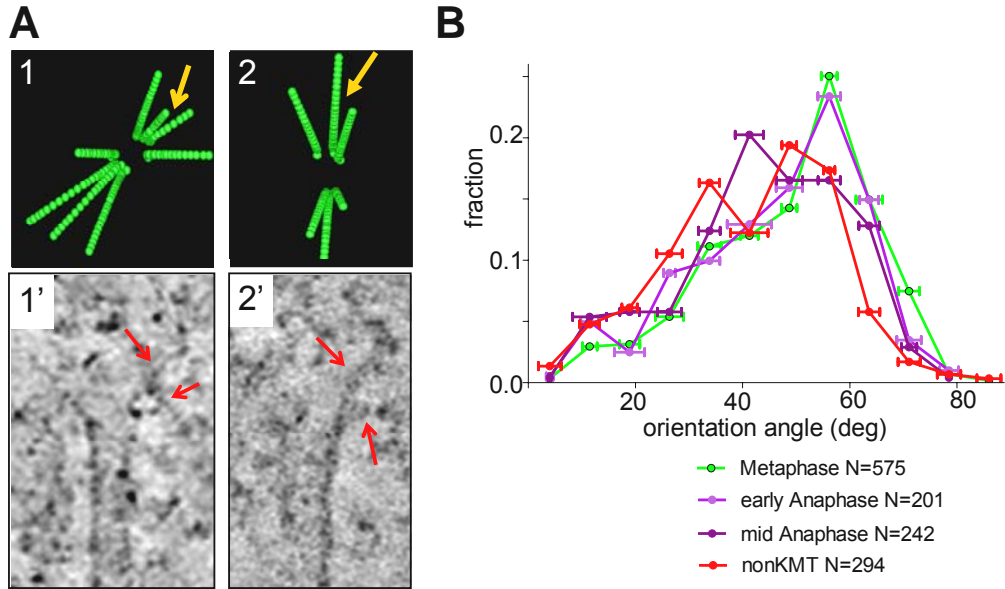
Figure S2. Details of PF structure: shape of adhering PFs (A) and orientation angles during mitotic progression (B). Panel **(A)** shows images of PFs from two metaphase KMTs with apparently adhering PFs, viewed along their axes in panels 1,2 (model views) and in perpendicular views as tomographic slices in panels 1',2'. PFs were scored as adhered if the angle between two adjacent tracings was significantly less than normal (~28°). Each such configuration was also viewed on its respective tomogram for closer examination (panels 1', 2'). Arrows indicate PFs that appear to be branched because they are sufficiently close that they are both seen in the single 6 nm slice that is shown. Graph in **(B)** shows distributions of orientation angles, as defined in Fig. 3C, box, for PFs from several stages of mitosis. Error bars are SEMs for each bin. The similarity of these distributions for KMTs from metaphase and early anaphase (sister chromatids just detectably separated) is striking. The distribution of orientations changes slightly as anaphase progresses (sister chromatids well separated and anaphase chromosomes about half-way to the spindle poles).
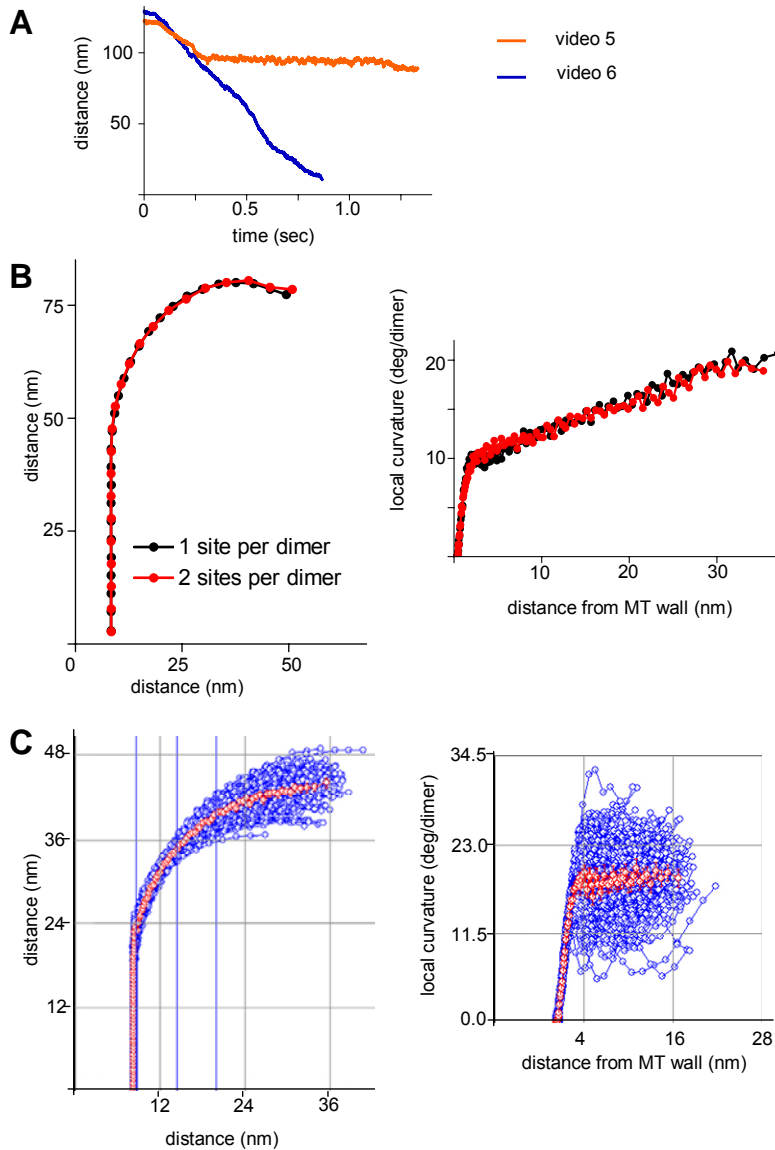
Figure S3. Computed motions of a load, which is coupled by fibrils to a depolymerizing MT. (A) shows position vs. time for the motion of a 40 pN load pulled by KFs that are bound weakly ($k_+ = 25$ sec^{-1}, orange curve) or strongly ($k_+ = 50$ sec^{-1}, blue curve) to PFs. Weak binding leads to the loss of many KF-PF associations, so the net pull from the depolymerizing MT is not sufficient to keep the load moving. Stronger binding leads to processive movement because all the PFs stay engaged. **(B)** Graphical representations of the effect of having one or two KF binding sites per dimer, as calculated from the model presented in Sup. Mat., Part 2. Unlike the model of the Dam1-like ring (Efremov et al., 2007), the KF-based coupling is insensitive to the number of the KF attachment sites per dimer, at least with respect to the average PF shape (left) and distribution of local curvature (right). **(C)** PF shape (left) and local curvature as a function of distance from the MT wall (right) for some of the theoretical PFs that were obtained in a numerical experiment shown on video 6; individual PFs and their local curvatures are blue and their averages are red. These graphs demonstrate that the stochastic variations in PF shape are significant, and they are greater for PFs segments farther from the MT wall.
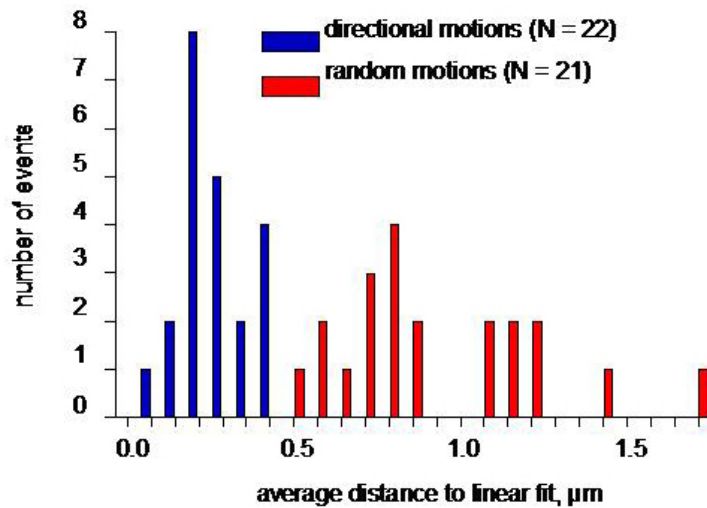
Figure S4. Analysis of motions of beads coated with Ndc80. Since some Ndc80 beads moved only short distances before detaching (0.5 – 1 μm), it was difficult to determine whether these motions were associated with depolymerizing MT ends or were random. To deal with this problem we fitted the trajectories for all beads in question with linear regression lines and then measured the shortest distances from each such line to the bead's center during its motion along this path. Now the average distance from this line could be calculated for each bead. The analogous procedure was then applied to similarly prepared beads that we knew were moving randomly. The distances for the latter beads were > 0.4. We therefore concluded that the experimental beads for which these distances were < 0.4 moved non-randomly with a probability > 1/N (or 95%), where N=21, the number of randomly moving beads we examined.
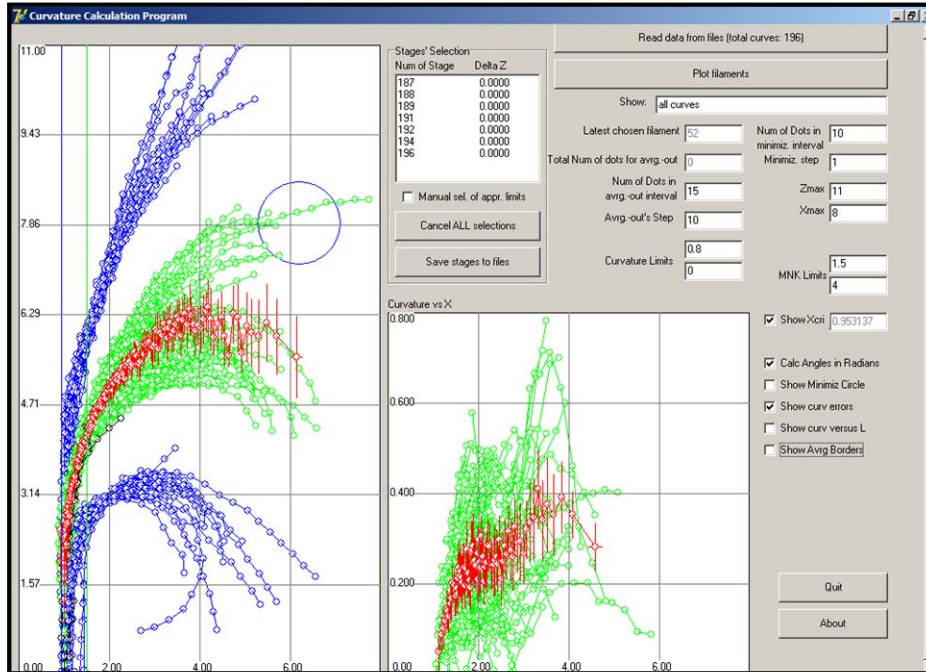
Figure S5. Screen Shot of the controls for the program that analyzes PF curvature (CCP).
For analysis and comparison, all PFs from a given class of MTs, e.g., KMTs from an early
anaphase PtK$_1$ cell as shown here, were extracted as 2D points by the *howflared* program in
IMOD and displayed on a single frame of reference. The PFs could then be sorted, either
manually or by some objective criterion like the average orientation of their segment for a
chosen distance from the MT wall, e.g. 6 - 12 nm, and then considered groups. Local curvature
as a function of distance from the MT wall was computed and displayed (green lines, central
panel) with mean values and standard deviations in a different color (red) (See Sup. Mat., Part 3
for description of algorithms). Mean positions with their deviations (left panel, red) could also be
displayed. The identifiers of all PFs from the original tomogram were preserved, so members of
any given class could then be extracted as image files from the original tomograms. This
program and detailed instructions for its use are available from
http://www.fazly.ru/index.php/en/software/.

Part 2. *Mathematical Description Of The Kinetochore-Associated Fibrillar Coupler And Its Interaction With A Microtubule.*

Table S9. Parameters and variables used for fibril description in the theoretical model

Model parameters	
l_i	length of the ith fibril
k_{fibr}	parameter that characterizes longitudinal stiffness of fibrils
N_{tot}	total number for fibrils
k_+	association rate constant for interaction between one fibril and a tubulin dimer
σ	fibrils density at the kinetochore
Model variables	
z_{kin}	z coordinate of the kinetochore disk
Δl_i	the length change for i^{th} fibril
Energy Potentials	
q_i	energy of longitudinal deformation for the ith fibril
U	full potential energy for fibrils-MT system

Model description. A microtubule (MT) is modeled as in (Molodtsov et al., 2005a) with the modifications described in (Efremov et al., 2007). The values of all model parameters that describe tubulin-tubulin interactions are same as in (Efremov et al., 2007): A = 28 k_BT, B = 300 k_BT/Rad, $\chi_o^{\alpha,\beta}$ = 0.2 Rad, r_o = 0.08 nm. Parameters of Dam1 ring interaction with MT are: r_{DAM} = 0.14 nm, k_{spring} = 0.13 N/m, k_{flex} = 20 k_BT/Rad, k_{DAM} = 13 k_BT. In calculations shown on videos 5 and 6, the plus end dimers detach from curled PFs when their bending angle $\tau_{k,n}$ > 2 Rad.

The kinetochore is modeled as a plane disk, whose position is defined by 6 coordinates: 3 angles and 3 Cartesian coordinates of the disk's mass center. We assumed that the disk was perpendicular to MT axis and did not rotate around this axis. Furthermore, in our system of coordinates the center of the mass for the disk lies at $x = 0$, $y = 0$. Hence only one of the disk's coordinates, the z coordinate of the center of the mass, is a variable in this model.

The kinetochore interacts with the tubulins in the outer wall of a straight MT or the separated PFs at the MT ends via elastic fibrils. Parameter N_{tot} describes total number of fibrils in the model. One end of each fibril is attached to the kinetochore and the other end extends toward the MT. The fibril is a flexible, linear elastic element that can stretch along its length with stiffness k_{fibr}. We assumed that the kinetochore-distal end of the fibril had a specific tubulin-

11

binding site, one per tubulin dimer. Models that assumed one binding site per tubulin monomer produced similar results; e.g. with respect to the predicted shape of the PF bending under tension (Fig. S3B) and the rate of kinetochore disk movement (not shown). In calculations below we assume that the fibril attaches at the center of the outer surface of the β-tubulin monomer but the exact position of the binding site on tubulin surface is not important for model conclusions. The binding takes place if the distance between this binding site and the kinetochore disk is less than or equal to the resting length of the fibril. When the binding site is occupied by one fibril, it cannot bind additional fibrils. The association rate constant for a fibril binding to tubulin is k_+ (sec^{-1}). For simplicity we assumed, that fibril dissociation from the tubulin occurred only after this dimer detached from the depolymerizing MT end.

Energy relationships. The fibrils deformations are described as elastic, half-Hookian springs. Thus, the energy of longitudinal deformation, q_i, for i-th fibril is given by

$$\begin{cases} q_i(\Delta l_i) = \dfrac{k_{fibr}}{2}\Delta l_i^2, & \Delta l_i > 0 \\ q_i(\Delta l_i) = 0, & \Delta l_i \leq 0 \end{cases}$$

where k_{fibr} is the fibril's longitudinal stiffness; Δl_i is the change in the length of i-th fibril and is a function of all independent model variables. The full potential energy for all fibrils-MT interactions, U, is therefore:

$$U = U_o(z) + \sum_{n=1}^{13}\left(\sum_{k=1}^{N_k}\left(g_{k,n}\left(\chi_{k,n}\left(\tau_{k,n}\right)\right) + v_{k,n}\left(r_{k,n}\left(\tau_{k,n}\right)\right)\right)\right) + \sum_{m=1}^{N_{tot}} q_m\left(\Delta l_m\left(z_{kin}, \tau_{k,n}\right)\right)$$

Here, $U_o(z)$ describes the applied tension; the second part describes the deformation energy of all PFs ($g_{k,n}$ is the energy potential for longitudinal bond between k^{th} and $(k-1)^{th}$ monomers in n^{th} PF, $\chi_{k,n}$ is the angle between k^{th} and $(k-1)^{th}$ monomers in n^{th} PF, $\tau_{k,n}$ is the angle between k^{th} monomer in the nth PF and MT's axis (vertical, plus end pointing up), $v_{k,n}$ is the potential for lateral bond between k^{th} monomers in n^{th} and $(n-1)^{th}$ PFs, $r_{k,n}$ is distance between lateral interaction points of kth monomers in n^{th} and $(n-1)^{th}$ PFs (see Molodtsov et al., 2005a and b, Efremov et al., 2007 for details)). The third part of this equation describes the deformation energy of kinetochore fibrils (Table S9).

Choice of model parameters. The total number of fibrils in the model (N_{tot}) depends on fibrils density σ (nm^{-2}) at the kinetochore: $N_{tot} = S \cdot \sigma$, where S is the kinetochore's area. The current model examines interactions between the kinetochore and a single depolymerizing MT. Hence, the kinetochore's area is chosen as a minimal area that completely "covers" the flared MT end: the ram's horns on a 25 nm MT occupy $\leq 100 \times 100$ nm^2 area, so S is 10^4 nm^2. When tightly packed, this area could bind up to ~400 globular proteins that are similar in size to, for example, tubulin. If each of these protein domains has a fibrillar "tail", the corresponding area will have a density similar to a solid object. Since electron micrographs of the kinetochore-MT attachment sites do not show such densely packed structures around the flared PFs, the number of the fibrils per kinetochore area in our model was chosen < 400. $N_{tot} = 50$ (one fibril per 200 nm^2 area) was sufficient to enable processive motion (for high fibril-tubulin affinity), so all results shown in this work were calculated for this parameter value.

Fibril length (parameter l_i) is chosen large enough, so that the fibril deformations are mostly co-axial with the MTs (i.e. the fibrils are oriented almost parallel to the MT axis). All

calculations described below were carried out for $l_i = 80$ nm, but the conclusions are unchanged for a wide range of l_i, so long as the lengths are greater than 25 nm, a diameter of MT.

Model calculations have shown that 10-fold variations in the longitudinal stiffness parameter, k_{fibr}, also have little effect on model solutions (not shown). Reduced stiffness increased the noise in kinetochore movement, but the speed of movement for a given opposing tension remained the same. Therefore, in all calculations here the value of this parameter was fixed: k_{fibr}=0.06 N/m. For a fibril l_i= 80 nm long with a cross-section of 10 nm^2, the corresponding Young modulus is E = $5 \cdot 10^8$ N/m^2; this value is close to the experimentally obtained value of the Young modulus for MTs (Munson et al., 2007). The viscosity of medium in the model is $5 \cdot 10^{-3}$ Pascal·sec. The value of the parameter k_+ was varied in calculations to examine the effect of binding strength for the fibril-tubulin interaction on the processivity of motion.

Model results. Calculations were carried out using the Monte Carlo-Metropolis method (Heermann, 1990), as described in (Efremov et al., 2007). The calculated positions of the kinetochore disk and coordinates of all tubulin monomers in the MT were recorded at 1 kHz. Fig. S3A shows changes of the disk's position with time when a 40 pN force was applied to the disk in the direction opposite to MT shortening. When the fibril-tubulin association constant was relatively high ($k_+ = 50$), the disc moved processively with roughly constant velocity (Video 6). The small oscillations in disk's position were caused by random fluctuations in fibril length, which in turn were caused by the stochasticity of PFs bending. Fig. S3C shows randomly selected examples of the calculated profiles for depolymerizing PFs for the same numerical "experiment" as on Video 6; the graph on the right shows the curvatures of these PFs. Clearly, the amplitude of the changes in the PF shape is quite high, which explains the observed small irregularities in disk movement.

We calculated the average shape of the PFs and the corresponding local curvatures by using about 200 randomly selected PFs for each numerical "experiment" and with the help of our custom-written "Curvature Calculation Program" (CCP) (Suppl. Mat, Part 3). Such an approach allowed us to determine the average shape of PFs for different model assumptions (such as the number of binding sites per tubulin dimer, Fig. S3B) or when the disk was subjected to a range of opposing tensions (Fig. 5A). Since this opposing tension was applied uniformly to the disk, 1/13th of the load could be attributed to each PF. When there is no tension, the predicted shape of the PF matches closely the shape of PFs on MTs depolymerizing in vitro (Fig. 5B). With increased opposing tension, the PF begins to straighten, especially in its segment closest to the MT wall (Fig. 5B,C). When a ring-shaped coupler is used (modeled as in Efremov et al., 2007 with $k_{DAM} = 13$ k$_B$T) under the uniform opposing load of 30 pN, which is close to the maximal load it can hold, PF shape does not change appreciably (Fig. 5B). The deformations are all localized to the PF regions 4-5 nm from the MT wall, where the PFs lean on the ring. The resulting changes are barely noticeable on the scale of this graph.

A fibril-based coupler can in principle support processive cargo motion for a large range of opposing tensions (Fig. 5A). When the load is small (< 10 pN per MT), the rate of kinetochore disc movement is almost the same as that of a freely shortening MT. Thus, this geometry of coupler has almost no "internal friction", a feature that distinguishes it favorably from the ring coupler (Efremov et al., 2007). With increasing load the rate of cargo motion decreases; it stalls asymptotically at a load of about 80 pN (6 pN per PF). This implies that a fibrous coupler can in principle transduce up to 100% of the energy that is stored in a stable MT. Even at this high load,

the motion will remain processive, so long as the fibril-tubulin binding is strong ($k_+ \geq 50$ sec^{-1}), which ensures that each of the 13 PFs remains attached to at least one fibril at any moment. Thus, a fibrous coupler takes advantage of the strain-dependency of tubulin dimer dissociation from the shortening MT end. The restraining properties of a coupler on PF bending and therefore tubulin dissociation dynamics were suggested in (McIntosh et al, 2002), and such an effect was detected experimentally with in vitro-based systems (Grishchuk et al., 2005; Franck et al., 2007).

Part 3. *A Computer Program for Quantitative Analysis of Shape of the Tubulin PFs.*

To analyze fine details of the shape of experimental and theoretical PFs we have designed software called the "Curvature Calculation Program" or CCP. CCP is written with Borland Delphi 7 medium for MS Windows 98 or higher, and it does not require any additional computer programs. Intel Pentium4 3000 MHz, AMD Athlon64 3200+ or newer processors are recommended. The program uses text files with the coordinates of the PFs, either acquired by tracing of the electron microscopic images with IMOD or as an output from numerical model calculations. The program window opens such files by showing all or a subset of the PFs selected by a user. The user can use mouse to move PFs relative to each other and organize them in groups (Fig. S5, PFs shown in blue in the left graph of the window). The selected group (Fig. S5, PFs in green) can then be used to calculate the shape of average PF (shown in red with error bars), as well as to view the local curvature of individual PFs in this group and their averages (green and red traces respectively in the graph on the right). These results can be saved in an output text file, if necessary.

CCP calculates average PF shape for a selected group of PFs by computing the mean and its deviation for horizontal (X) and vertical (Z) coordinates within a user-defined segment, starting from (0,0); analogous procedures are then carried out for segments that are shifted by a user-defined step until reaching the end of the longest PF in this group. We routinely calculated the average shape for a group of 40-50 PFs, using the segments with 10-20 coordinates and step size 1.

Local curvature of a segment of the PF was calculated with a least-squares method that uses arcs with variable radii to achieve the best fit to the PF segment of the user-defined size. The inverse value of this radius was used as a curvature for this PF segment. All values for the local PF curvatures cited in this paper were calculated as above but then adjusted so that they represent the angular deviation between two adjacent, linear segments 8 nm long (therefore, measured in degrees per dimer length).

Finally, the CCP was used to calculate the orientation angles for the PF segments at a given distance from the MT wall (0,0). Such a distance interval is specified by a user, then the program uses a least-squares method to calculate the linear segment that fits best the selected PF segment. The angle between this linear segment and the horizontal axis is then calculated.

Supplemental References

Belmont, L. D., A. A. Hyman, K.E. Sawin, T.J. Mitchison (1990). Real-time visualization of cell cycle-dependent changes in microtubule dynamics in cytoplasmic extracts. Cell **62**(3): 579-89.

Dong, Y., Vanden Beldt, K. J., Meng, X., Khodjakov, A. and McEwen, B. F. (2007). The outer plate in vertebrate kinetochores is a flexible network with multiple microtubule interactions. Nat Cell Biol **9**, 516-22.

Efremov, A. K., Grishchuk, E. L., McIntosh, J. R., and Ataullakhanov, F. I. (2007). In search of an optimal ring to couple microtubule depolymerization to processive chromsome motions. Proc Natl Acad Sci U S A **104**(48): 19017-22.

Franck, A. D., A. F. Powers, Gestaut, D. R., Gonen, T., Davis, T. N., C. L. Asbury (2007). "Tension applied through the Dam1 complex promotes microtubule elongation providing a direct mechanism for length control in mitosis." Nat Cell Biol **9**(7): 832-7.

Heermann, D. W. Computer Simulation Methods in Theoretical Physics (Springer-Verlag, New York, 1990).

Grishchuk, E. L., M. I. Molodtsov, Ataullakhanov, F. I., and J. R. McIntosh (2005). "Force production by disassembling microtubules." Nature **438**(7066): 384-8.

McIntosh, J. R., E. L. Grishchuk, and R.R. West (2002). "Chromosome-microtubule interactions during mitosis." Annu Rev Cell Dev Biol **18**: 193-219.

Molodtsov, M. I., Ermakova, E. A., Shnol, E. E., Grishchuk, E. L., McIntosh, J. R., and Ataullakhanov, F. I. (2005a). A molecular-mechanical model of the microtubule. Biophys J **88**, 3167-3179.

Molodtsov, M. I., Grishchuk, E. L., Efremov, A. K., McIntosh, J. R., and Ataullakhanov, F. I. (2005b). Force production by depolymerizing microtubules: a theoretical study. Proc Natl Acad Sci U S A **102**, 4353-4358.

Munson, K.M., P.G. Mulugeta, and Z.J. Donhauser (2007). "Enhanced mechanical stability of microtubules polymerized with a slowly hydrolyzable nucleotide analogue." J Phys Chem B **111**: 5053-7.

Rusan, N.M., C.J. Fagerstrom, A.M. Yvon, P. Wadsworth (2001). "Cell cycle-dependent changes in microtubule dynamics in living cells expressing green fluorescent protein-alpha tubulin." Mol Biol Cell **12**(4): 971-80.

VandenBeldt, K. J., Barnard, R. M., Hergert, P. J., Meng, X., Maiato, H., and McEwen, B. (2006). Kinetochores use a novel mechanism for coordinating the dynamics of individual microtubules. Current Biol **16**, 1217-1223.